Uniformity of Imaging Spectrometry Data Products

Jens Nieke, Daniel Schläpfer, Francesco Dell'Endice, Jason Brazile, and Klaus I. Itten, *Senior Member, IEEE*

***Abstract*—The increasing quantity and sophistication of imaging spectroscopy applications have led to a higher demand on the quality of Earth observation data products. In particular, it is desired that data products be as consistent as possible (i.e., ideally uniform) in both spectral and spatial dimensions. Yet, data acquired from real (e.g., pushbroom) imaging spectrometers are adversely affected by various categories of artifacts and aberrations including as follows: singular and linear (e.g., bad pixels and missing lines), area (e.g., optical aberrations), and stability and degradation defects. Typically, the consumer of such data products is not aware of the magnitude of such inherent data uncertainties even as more uncertainty is introduced during higher level processing for any particular application. In this paper, it is shown that the impact of imaging spectrometry data product imperfections in currently available data products has an inherent uncertainty of 10%, even though worst case scenarios were excluded, state-of-the-art corrections were applied, and radiometric calibration uncertainties were excluded. Thereafter, it is demonstrated how this error can be reduced ($< 5\%$) with appropriate available technology (onboard, scene, and laboratory calibration) and assimilation procedures during the preprocessing of the data. As a result, more accurate, i.e., uniform, imaging spectrometry data can be delivered to the user community. Hence, the term uniformity of imaging spectrometry data products is defined for enabling the quantitative means to assess the quality of imaging spectrometry data. It is argued that such rigor is necessary for calculating the error propagation of respective higher level processing results and products.**

***Index Terms*—Calibration, data processing, imaging, spectroscopy.**

I. Introduction

Since the first airborne hyperspectral imagers (HSIs) were developed in the 1980s, significant effort has been devoted to increase the quality of the resulting hyperspectral data cube. Today, it can be stated that the use of hyperspectral data found its way from prototyping to commercial applications resulting in an increasing demand on highly accurate measurements to satisfy the needs of hyperspectral data user community [1]. In general, a hyperspectral data cube is typically generated by a pushbroom- or whiskbroom-type imaging spectrometer in order to enable the registration in the three dimensions of the cube, i.e., spectral, first spatial (across-track), and second spatial time (along-track) domains [2]. Examples for selected currently operational [3]–[8] and soon-to-be-available HSI [9]–[11] are given in the Table I.

Even though HSI instrument development and its data application have long history, error estimations for the entire data cube were not established so far—mainly due to the lack of detailed performance specifications on the manufacturer side and the nescience of the consequence of relaxed (or nonexisting) requirements on the user side.

In order to better understand the quality of the HSI data products, a thorough understanding of nonuniformities of the data and their corresponding correction schemes needs to be elaborated.

This is why this paper specifically performs the following:

1) addresses the HSI instrument model, which was developed at Remote Sensing Laboratories (RSL) in order to account for the error contributions of data nonuniformities appropriately;
2) describes the source and impact of uniformities artifacts on the HSI data products quality;
3) outlines possible characterization, calibration, and correction schemes;
4) summarizes the overall impact on the HSI product and gives estimates on anticipated errors.

II. Instrument Model

An appropriate HSI instrument model F is introduced for serving as a forward model in order to solve the inverse problem of data processing as well as that of instrument calibration.

The instrument model must reproduce the instrument's behavior accurately. This is why, first, the common equation of signal transformations is provided. The transformation converts the digital numbers C inside the instrument to the radiance field L_s

$$C = F * L_s \tag{1}$$

where the symbol $*$ represents the convolution operator.

Due to the higher transformation complexity of a pushbroom-like HSI, only this kind of instrument is addressed in this paper. In an HSI optical system, the photons of the radiance at sensor L_s are distributed among the pixels of the detector in both the spectral and the across-track directions. The forward movement of the instrument over the scene and the detector's integration time—together with high frequency read-out—allows generation of a hyperspectral data cube.

The instrument model consists of the system's pixel response function $R_{\mathrm{sys}}^{\mathrm{PRF}}$ and various other calibration and characterization parameters (such as polarization sensitivity, ghost and

Manuscript received June 4, 2007; revised September 29, 2007. First published Month 00, 0000; last published Month 00, 0000 (projected).

J. Nieke is with the European Space Agency (ESA), European Space Research and Technology Centre, 2200 Noordwijk, Netherlands.

D. Schläpfer is with the Remote Sensing Laboratories (RSL), University of Zurich, 8057 Zurich, Switzerland, and also with Kantonsschule Wil, 9501 Wil, Switzerland.

F. Dell'Endice, J. Brazile, and K. I. Itten are with the Remote Sensing Laboratories (RSL), University of Zurich, 8057 Zurich, Switzerland.

Color versions of one or more of the figures in this paper are available online at http://ieeexplore.ieee.org.

Digital Object Identifier 10.1109/TGRS.2008.918764

TABLE I
SPECIFICATIONS AND DESIGN PARAMETERS FOR CURRENT AND FUTURE HYPERSPECTRAL IMAGERS

HSI [manufacturer, country/agency]	Year of 1st operations	No. of Spectr. Bands	Spectr. Range (µm)	Spectr. Resolution (λ/Δλ)	FOV [deg] IFOV [mrad]	Imaging Technique
Airborne IS						
AVIRIS [JPL, US]	1987	224	0.4 - 2.5	40-200	30° 1 mrad	1D whisk., grating
CASI [ITRES, CA]	1990	288	0.4 - 1.0	200	40° 1.5 mrad	2D push., grating
HYMAP [Intergrated Spectronics, AU]	1994	128	0.4 - 2.5	30-125	65° 2 mrad	1D whisk., grating
AISA Eagle [SPECIM, FI]	2005	244	0.4 - 0.97	200-300	39.7° 1 mrad	2D push., prism
ARES [Intergrated Spectronics, AU/DLR]	from 2007	128 (VIS-SWIR); 30 (TIR)	0.4-2.5 8-12	30-125 64-100	65° 2 mrad	1D whisk., grating
APEX [RUAG, ESA/CH/BE]	from 2008	313-500	0.38 - 2.5	1000-277	28° 0.5 mrad	2D push., prism
Spaceborne IS						
HYPERION [Northrop Grumman, NASA]	2000	200	0.4 - 2.5	40-250	7.5 km, 30 m	2D push., grating
CHRIS [SSTL, ESA]	2001	18-62	0.4 - 1.0	300-90	13km, 17-34 m	2D push., prism
EnMAP [Keyser Threde, GFZ, DLR]	from 2012	220	0.43 - 2.5	43-250	30km, 30m	2D push., prism

straylight effects, and the absolute radiometric accuracy) combined in the variable K_{sys}

$$F = R_{\mathrm{sys}}^{\mathrm{PRF}} * K_{\mathrm{sys}}. \tag{2}$$

Assuming a linear system, the $R_{\mathrm{sys}}^{\mathrm{PRF}}$ can be expressed as a multiple convolution of point spread functions (PSFs), each associated with one of the system components (e.g., the optics, detectors, and signal and data processing).

In the case of a pushbroom imaging spectrometer, the image of one line is redistributed at the detector level in the spectral (λ) and first spatial (θ) domains. Together with the along-track movement (given by the time t) of the sensor (second spatial domain), we define two spatial PSFs ($R_{\mathrm{AC}}^{\mathrm{PSF}}$ and $R_{\mathrm{AL}}^{\mathrm{PSF}}$) and the spectrometer-inherent spectral response function (SRF) $(R_{\lambda}^{\mathrm{SRF}})$. The convolution of the normalized PSFs (in a way that the 2-D integral over the two-orthogonal distance variables is equal to one) and the $R_{\lambda}^{\mathrm{SRF}}$ results in the pixel response function $(R_{\mathrm{IS}}^{\mathrm{PRF}})$

$$R_{\mathrm{IS}}^{\mathrm{PRF}} = R_{\mathrm{AC}}^{\mathrm{PRF}} * R_{\mathrm{AL}}^{\mathrm{PRF}} * R_{\lambda}^{\mathrm{SRF}} \tag{3}$$

where $R_{\mathrm{AC}}^{\mathrm{PSF}}$ and $R_{\mathrm{AL}}^{\mathrm{PSF}}$ correspond to the across-track (indices AC) and along-track (indices AL) PSFs.

Hence, $R_{\mathrm{IS}}^{\mathrm{PRF}}$ is the spatial map of sensitivity across a pixel as well as the information about the crosstalk between neighboring pixels over the entire detector at a certain wavelength λ.

Now, the relation for the HSI needs to be expressed mathematically. In contrast to classical camera design models [12], [13], an HSI model must also account for the spectral domain, resulting in an incident image intensity distribution represented by $f(x, y, z)$, with the pixel response function $r(x, y, z)$ and the signal $s(t, \lambda, \Theta)$ being detected by the pixel (i, j, k) and given as

$$s(i, j, k) = \iiint_{-\infty}^{+\infty} L_s(t, \lambda, \theta) F_{i,j,k}(t, \lambda, \theta) dt d\lambda d\theta \tag{4}$$

on the level of the detector.

The data are already influenced by the optics, and therefore, the different equation based on the image density function $f(x, y, z)$ applies

$$s(i, j, k) = \iiint_{-\infty}^{+\infty} R_{\mathrm{sys}}^{\mathrm{PRF}}(x, y, z) f(x, y, z) dx dy dz \tag{5}$$

where the coordinate system is defined with reference to the detector.

The R^{PRF} resulting from the convolutions in the two spatial and the spectral domains is a good basis to assess the quality of HSI data. Here, the shape, the size, and the diameter of the central lobe are not only related to the spectral and spatial resolutions but also to the sharpness in 3-D of the image cube produced. An ideal R^{PRF} would have a constant value within the boundaries of a pixel (i.e., uniform pixel sensitivity) and

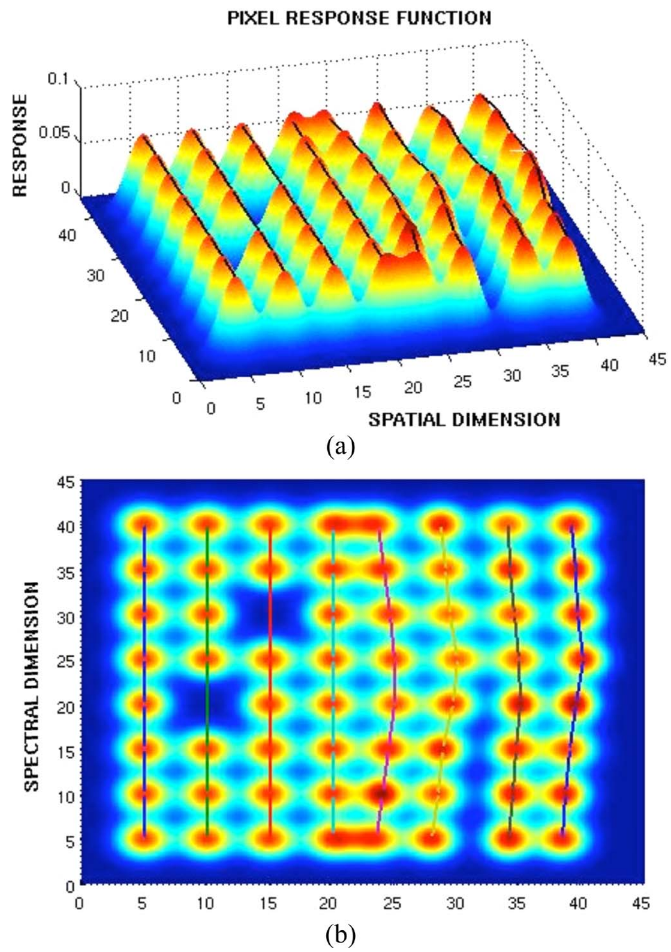

Fig. 1. 3-D view (a) and top view (b) of PRF for eight across-track pixels and eight spectral bands before the 2-D detector array. On the left side, 4 × 8 PRFs are uniform except of two bad pixels. In contrast, keystone (or spatial misregistration) as nonuniformity is affecting the image quality of 4 × 8 PRFs on the right side.

zero outside (i.e., no crosstalk or oversampling). However, in practice, instrument data show intrapixel sensitivity variations and nonuniformities in the detector domains (see Figs. 1 and 2). This is why real sensors' PRFs are, in general, simplified as Gaussian functions and not as boxcar functions—the Gaussian distribution more closely matches the description of real sensors. However, we have to keep in mind that the Gaussian PSF is still a simplification. The differences to a real PSF can be estimated comparing the function shapes in Fig. 1 for Gaussian and Fig. 2 for real system distributions.

For the components of R^{PRF} to be measured, various techniques can be applied. Whereas monochromators, tunable lasers, echelons, or absorption filters can be used for R^{SRF} determination, the characterizations of $R^{\mathrm{PSF}}_{\mathrm{AC}}$ and $R^{\mathrm{PSF}}_{\mathrm{AL}}$ are more complex. A favorable way is to characterize the PSF via a line spread function (LSF) (R^{LSF}) or an edge spread function (R^{ESF}). In contrast to the PSF, which can be regarded as a two-dim response to an input point source, the one-dim LSF is determined by a line that is infinitely long and narrow. However, either an R^{LSF} or R^{ESF} exists for each line or edge orientation. Assuming that $R^{\mathrm{PSF}}_{\mathrm{AC}}(y,z)$ represents the response at a point of the spatial coordinate (y,z) and that $R^{\mathrm{LSF}}_{\mathrm{AC}}(y')$

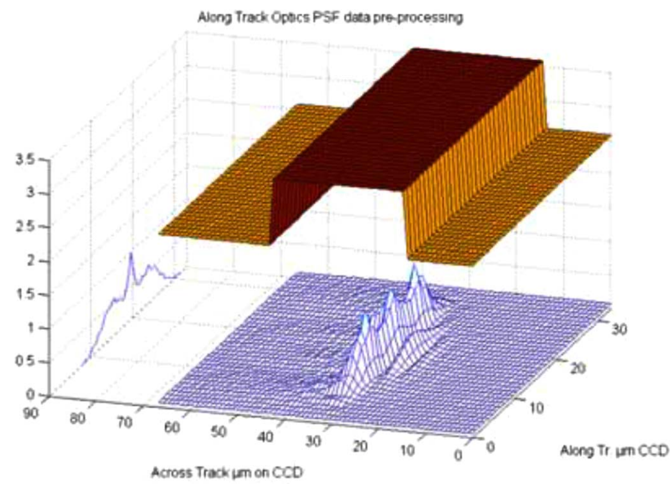

Fig. 2. Typical PSFs as an $R^{\mathrm{PSF}}_{\mathrm{AC}} * R^{\mathrm{PSF}}_{\mathrm{AL}}$ convolution for an imaging spectrometer at $\mathrm{FOV} = 14°$ and $\lambda = 400$ nm.

represents the LSF for a line of orientation z', where y' is orthogonal to z', then the LSF is the integral of the $R^{\mathrm{PSF}}_{\mathrm{AL}}$ in the z'-direction

$$R^{\mathrm{LSF}}(y') = \int_{-\infty}^{+\infty} R^{\mathrm{PSF}}_{\mathrm{AC}}(y,z)\,dz'. \tag{6}$$

The straightforward consequence of (1)–(6) is that $R^{\mathrm{PRF}}_{\mathrm{IS}}$ should be exactly known in order to decompose the measured data C into a sum of point sources with known spatial and spectral profiles, i.e., the quantitative assessment of the quality of HSI data.

To better understand the influence of possible imperfections of a homogenous or uniform distribution of equal $R^{\mathrm{PRF}}_{\mathrm{IS}}$, it is important to define the artifacts and aberrations in HSI data and their consequences more precisely.

III. Impact of Uniformity Defects on Imaging Spectrometry Data Products

A. *Uniformity Definition*

Two uniformity terms are commonly used for the description of artifacts in electronic imaging, i.e., spatial uniformity and temporal uniformity.

1) Spatial uniformity: For spatial uniformity, the radiometric response is defined as equality within a (spatial) frame detector. This term primarily stems from frame imaging, e.g., in digital photography. It includes effects such as striping or spectrally variable radiometric response related to varying quantum efficiency within a detector array.
2) Temporal uniformity: The temporal uniformity describes the temporal radiometric response stability of a detector element. This term is common in video analysis and is used synonymously with "radiometric stability" in imaging spectroscopy.

In contrast to those definitions, pushbroom imaging spectrometry consists of one image frame registering the spectral and the spatial dimension simultaneously. Any nonuniformity in the system PSF (i.e., the PSF nonuniformity) leads therefore to nonuniformities of the data products in both the spectral and spatial dimensions [14]. Such nonuniformities are commonly termed smile and keystone, respectively. This is why the term uniformity of imaging spectrometry data products must be introduced.

B. Uniformity of Imaging Spectrometry Data Products

In order to reduce the $R_{\mathrm{IS}}^{\mathrm{PRF}}$ nonuniformity of HSI data, major efforts on data preprocessing and analysis have to be taken into account. The following types of imperfections are defined as nonuniformities, assuming the pixel as a point.

1) Singular defects, where the $R_{\mathrm{IS}}^{\mathrm{PRF}}$ of a single pixel is significantly lower (e.g., 50%) than the mean response of the surrounding detector pixels (e.g., "bad pixels"). Also, all intrapixel nonuniformities are singular defects that are not to be neglected for HSI data preprocessing.
2) Linear defects, where the response of an entire line is affected (e.g., "striping," missing lines) or smear [15].
3) Area defects, where the entire frame has imperfections, which are mainly formed by optical aberrations and sampling inconsistencies in the spectral and the first spatial domain. The result is a PSF nonuniformity through spectral and spatial misregistrations which correspond to smile and keystone within one detector array [16].
4) Stability defects, where the entire image cube (including the temporal dimension) is affected by, e.g., nonstability of an instrument. These defects typically result in deviations in the second spatial (along-track) domain during the flight.
5) Discontinuity defects are caused through the degradation of the HSI through stepwise deteriorations in the optics and/or electronics of the instrument. This defect may cause misinterpretations of temporal effects and time series.

C. Impact of Nonuniformity

After defining the nonuniformity of imaging spectrometry data, it is important to quantify the impact of the PSF nonuniformity on data processing. The most prominent effects have been analyzed recently, i.e., $R_{\mathrm{AC}}^{\mathrm{PSF}}$ variation, coregistration, and spectral stability, using test data, which were systematically convolved to standard $R_{\mathrm{AC}}^{\mathrm{PSF}}$ values. The root mean square (rms) of the radiance difference between deviating PSFs and an ideal PSF was derived from such simulated data, which resulted in relative error percentages. As test data, various spectral data cubes were used, such as artificial data cubes derived from the SPECCHIO spectral database [17], [18], where a wide range of more than 4000 natural and simulated surface reflectance spectra had been modeled to at-sensor radiance data using the MODTRAN radiative transfer code [19], or a number of real imaging spectrometry (e.g., from AVIRIS) test data sets. The results from the different analyses [14], [20] are summarized in the following.

1) Singular and Linear Defects: The correction of singular pixel defects was tested by linear interpolation of missing pixels from neighboring pixels. The average error of the bilinear interpolation method to the original pixel value was between 11% and 19% for the replacement of individual pixels, dependent on the wavelength and the interpolation method. If the interpolation was done in the spectral domain, this error was reduced below 5% for spectrally highly resolved instruments. The deviations with nearest neighbor processing were stable at about 17.5%. Bilinear interpolation performed better than nearest neighbor replacement techniques by a factor of up to two if only individual pixels have to be replaced. Singular defects could not be corrected by interpolation beyond a distance of two to three pixels for high-resolution imagery [20].

2) Area PSF Defects: For HSI, the spatial PSF width is ideally 1.0 and, typically, is slightly blurred to higher values assuming a contiguous sampling. A variation of the PSF width of 1–1.6 pixels in the across-track direction and 1.2–1.6 pixels in the along-track dimension across the full spectral range was investigated. The influence on the data is in the range of 1%–4% [14]. The results for PSF variations showed that higher resolution of low altitude imagery increases the errors significantly—this indicates that the highest resolution imagery will be even more critical.

Spatial coregistration between the two detectors (e.g., for a visible and infrared channel) can be defective due to pressure- or temperature-dependent misregistrations. In fact, this is a special case of area defects and may be treated by similar procedures. The misregistration effect is quantified as the standard deviation of the difference between resampled imagery using ideal and distorted sensor models. Relative differences of at-sensor radiance reaching 10% were observed between the two sensor models for an arbitrary collection of spectra. To improve the situation, across-track linear interpolation was applied to distorted data (at the same spatial resolution) in order to recover the original image positions. The linear interpolation reduced the error to a level of 2% [20].

3) Stability Defects: The stability of HSI is mainly driven by pressure/temperature dependencies resulting from flight level variations from airborne systems and solar heat forcing on the sensor during a single orbit for spaceborne systems. Deviations from uniformity may be observed in the data up to a corresponding estimated level of 10% (compare Table V). The quantification of this defect is technically feasible using an onboard characterization means and the HSI instrument model. A relative accuracy (i.e., stability) level of 2% is achievable by onboard characterization and subsequent data calibration—in case these instabilities are actually encountered [21], [22].

4) Discontinuity Defects: Discontinuities of system performance are by nature unforeseeable (e.g., degradation of optical performances) in their impact on system performance. It is assumed that laboratory or in-flight performance monitoring will allow tracing the system performance after a discontinuity has been encountered, e.g., after an unexpected shift of the system parameters. Except for a short transition phase, laboratory or in-flight calibration will allow a complete update of the system characterization. Depending on the performance of in-flight monitoring, a 2% error level can be reached, at the latest after a new laboratory characterization [20].

TABLE II
ESTIMATED IMPACT IN TERMS OF RMS DEVIATIONS DUE TO NONUNIFORMITIES FOR THE APEX INSTRUMENT

Non-Uniformity	Maximum Error	Corrected Error
Point / Line	16%	5%
Area: spatial PSF	4%	1%
Area: spectral PSF	5%	1%
Shortterm Stability	10%	2%
Longterm Discont.	50%	2%
Total RMS	**52.90%**	**6.3%**

TABLE III
TYPICAL TECHNICAL REQUIREMENTS FOR STATE-OF-THE-ART HSI [23], [24].

Dimension	Technical Requirement	EnMAP	APEX
Spectral	Spectral Misregistration	< 0.2 pixels	< 0.2 pixels
	Spectral Stability	< 0.5 nm	< 0.1 nm
Spatial	Spatial Misregistration	< 0.2 pixels	< 0.16 pixels
	Coregistration error (VNIR-SWIR)		< 0.16 pixels
General	Relative radiometric stability		< 2%

5) Error Budget: Such derived relative errors due to the different nonuniformity effects can be scaled to the actual performance of a specific HSI using a linear relationship between nonuniformity value and expected error. Given the expected radiometric performance of current systems (e.g., those mentioned in Table I), a residual inaccuracy in the range of 2% [21] is achievable for short-term stability only and remains a challenging goal for operational long-term use of the instrument.

In Table II, the impact of nonuniformities is summarized for the most prominent effects in terms of relative data errors as worst case maximum error and corrected error estimates. The residual error is large even after corrections are applied. It only falls below 4% if bad pixels are not part of the error budget or if considerably improved correction schemes are developed for all kinds of nonuniformities.

D. Typical Uniformity Requirements for HSI Data Products

The state of the art of technical requirements for PSF-related issues for HSI is quite difficult to determine since these values were not discussed in detail within the HSI user community so far. This is why just some state-of-the-art requirements can be summarized resulting from two exemplary sensors (Table III). Those values combined with the values retrieved from existing instruments using scene-based characterization methods (Section IV) will be used in Section V as average performance values.

IV. INSTRUMENT AND DATA CALIBRATION

Since the early steps of HSI calibration, important steps in the quantification of HSI nonuniformities have been performed [25], [26]. In order to deliver high-quality data products, it is necessary to quantify the defect and, thereafter, calibrate the flight data appropriately. These steps are called instrument calibration and data calibration. The realization is carried out during various calibration cycles and a processing of the flight data using the retrieved calibration parameters. In the following, an exemplary approach is described on how HSI instrument and data calibration is performed [22], [27] and the subsequent processing [28] is provided. This approach has been tested with various HSI data sets; it is also generic, i.e., can be used for different HSI sensors.

A. Calibration Measurements

First, the HSI instrument model F and the related parameters have to be described appropriately. Therefore, it is necessary to perform a large variety of calibration and characterization measurements applying different methods, e.g., onboard characterization, frequent laboratory characterization, and vicarious calibration. The retrieved parameters allow data calibration in a processing and archiving facility (PAF). The data calibration includes the calculation of the required time-dependent calibration coefficients from the calibration parameters and, subsequently, the radiometric, spectral, and geometric calibrations of the raw data. Because of the heterogeneity of the characterization measurements, the optimal calibration for each data set is achieved by using a special assimilation algorithm. In order to demonstrate state-of-the-art calibration technology, the characteristics of the recently developed calibration facilities are summarized in the following sections. Serving as examples are the APEX in-flight characterization (IFC) [22], [29] and the APEX calibration home base (CHB) facilities, which were recently developed and allow accurate PRF characterization measurements for providing input for the subsequent processing and assimilation scheme.

1) Onboard Performance Monitoring: As an integral part of an HSI, an onboard performance monitor can be used to perform characterization measurements using a filter wheel consisting of various filters, which permits spectral and radiometric characterization. The spectral filters are a rare-earth filter and three bandpass filters at 694, 1000, and 2218 nm. IFC design and performance were described recently [22], and it was shown that the IFC is capable of characterizing the spectral band center with an accuracy of < 1 nm together with a radiometric stability of $< 0.5\%$ as relative error. IFC measurements are performed before and after each run (flight line with continuous uninterrupted data acquisition) and during the CHB calibration measurements.

2) CHB: The CHB with dedicated spectral, radiometric, and geometric calibration facilities allows full laboratory characterization and calibration of HSI. The CHB is located at DLR in Oberpfaffenhofen near Munich (Germany).

The CHB consists of a large integrating sphere (1.6-m diameter) to enable radiometric calibration and an optical bench for the spatial and spectral calibrations of APEX. The entire setup makes use of a highly stable design mechanism, such as a rigid granite optical bench, a perfectly isolated foundation (seismic block), and special air bearings. This is why high positioning accuracy in the range of micrometers and arc seconds can be guaranteed. Details on the special design realized for the calibration bench, the integrating sphere, and the interfaces, as well as the large variety of possible spectral, geometric, radiometric, polarimetric, and straylight-related characterization measurements, are given in [29]. For the determination of APEX's PRF, the following measurements are performed: SRF and across/along-track LSF characterization.

For the SRF, a two-step procedure is applied. In the first step, the stimulus from a monochromatic source is geometrically centered on a detector column by equalizing the signal from neighboring elements. In the second step, the SRFs of the elements in this column are scanned by the stepwise increase or decrease of the wavelength of the stimulus. For each element, the integration time should be individually optimized by APEX to suppress noise and achieve best possible results.

Spatially, the characterization will be performed in along- and across-track directions by measuring the R^{LSF} simultaneously using the panchromatic beam of the collimator. For the characterization of the entire matrix detector, the measurements have to be performed for different angular positions across the swath.

For the along-track $R^{\mathrm{LSF}}_{\mathrm{AL}}$, the measurement will be accomplished by shifting a vertical slit (perpendicular to the one used for the across-track $R^{\mathrm{LSF}}_{\mathrm{AC}}$) in the focal plane of the collimator slightly left and right, i.e., in along-track direction. This movement will be realized by a rotating slit wheel, as the rotational component of such a small shift is negligible. The LSF for the across-track characterization is measured in steps of 1°, i.e., performing 29 steps from -14° to $+14^\circ$.

It has been recently shown [29] that the resulting accuracies of R^{LSF} and R^{SRF} characterizations are in the range of < 0.1 pixels leading to very small uncertainties with regard to spectral (± 0.1 nm) and geometric (± 0.007 mrad) calibrations.

3) Vicarious or Scene-Based Calibration: In-orbit vicarious or scene-based calibration is an important tool for monitoring an instrument's performance throughout the mission's duration. Along with the measurement of radiometric features, spectral R^{SRF} and spatial PSF characterizations and/or refinement can be performed as well. In support of the aforementioned uniformity goals, the latter two (R^{SRF} and R^{PSF}) are more critical and, therefore, led to a more detailed investigation. Based on proofs of concept, it has been shown that both R^{SRF} (i.e., band center, bandwidth, and R^{SRF} shape) and spatial misregistration (i.e., keystone) characterizations are possible in most cases. This is of special interest for addressing HSI nonuniformity issues, particularly for those instruments where characterization is only performed once throughout the entire mission duration, i.e., during the prelaunch calibration activities.

a) Spectral misregistration: While the scene-based retrieval of band center and bandwidth is well described in literature [30]–[34], recently, the discernibility of per-band SRF parameters has been explored using imaging spectrometry data [34]. It was demonstrated that various instrument R^{SRF} shapes could be discerned from a scene by measuring the difference between HSI data and various theoretical R^{SRF} (Gaussian, Bartlett, cosine, Welch, and box).

In particular, to establish discernibility, feature windows for comparison of 75 MODTRAN-4 cases (five target reflectances $\times$ three visibilities $\times$ five R^{SRF}) were selected from among candidate Fraunhofer lines determined to have prominent features: K (Ca), H (Ca), G (Fe), C (H), B (O_2), and A (O_2) (see Fig. 3). For each candidate feature, all window sizes ranging from two to five bands on each side of the feature were iteratively evaluated to choose the "best" window. The window size was then fixed for that particular feature, and an iterative window selection procedure allowed tuning the selection of features that are most suitable for a particular instrument.

In this investigation, it was shown that the Bartlett R^{SRF} is generally the least discernible from the Gaussian R^{SRF}; the A (O_2) and B (O_2) features seem to have the lowest signal-to-noise (SNR) requirements for discernment; the seemingly very similar cosine and Welch R^{SRF} appear to be easily discernible when compared against the Gaussian; and finally, differing visibility and target reflectance values have mostly minor influences on discernibility.

Based on the establishment of discernibility under these conditions, a method for direct R^{SRF} retrieval was then developed assuming less theoretical R^{SRF} shapes and tested over a wider variety of instrument performance characteristics [35]. Promising results were seen under simulation conditions, allowing variation of parameters over hundreds of permutations based on models of three currently available imaging spectrometers.

Promising results were seen under simulation conditions, allowing variation of parameters over hundreds of permutations based on models of the CHRIS, Hymap, and Hyperion imaging spectrometers, even though their realization of the feature window sizes and locations relative to the actual feature centers varied greatly. Many features proved usable with SNR performance as low as $5000:1$, which is easily achievable by averaging samples of topologically invariable homogeneous targets, since SNR is improved by the square root of the number of samples taken. Even in its currently primitive form, the described method could be used to obtain SRF estimates better than the typically used Gaussian for the not-uncommon case in which bands are created by summing up to tens of subchannels.

In summary, an instrument's R^{SRF} shape can now be added along with the already established bandwidth and band center in the list of spectral characteristics that can be retrieved or at least refined from the spectrometry data.

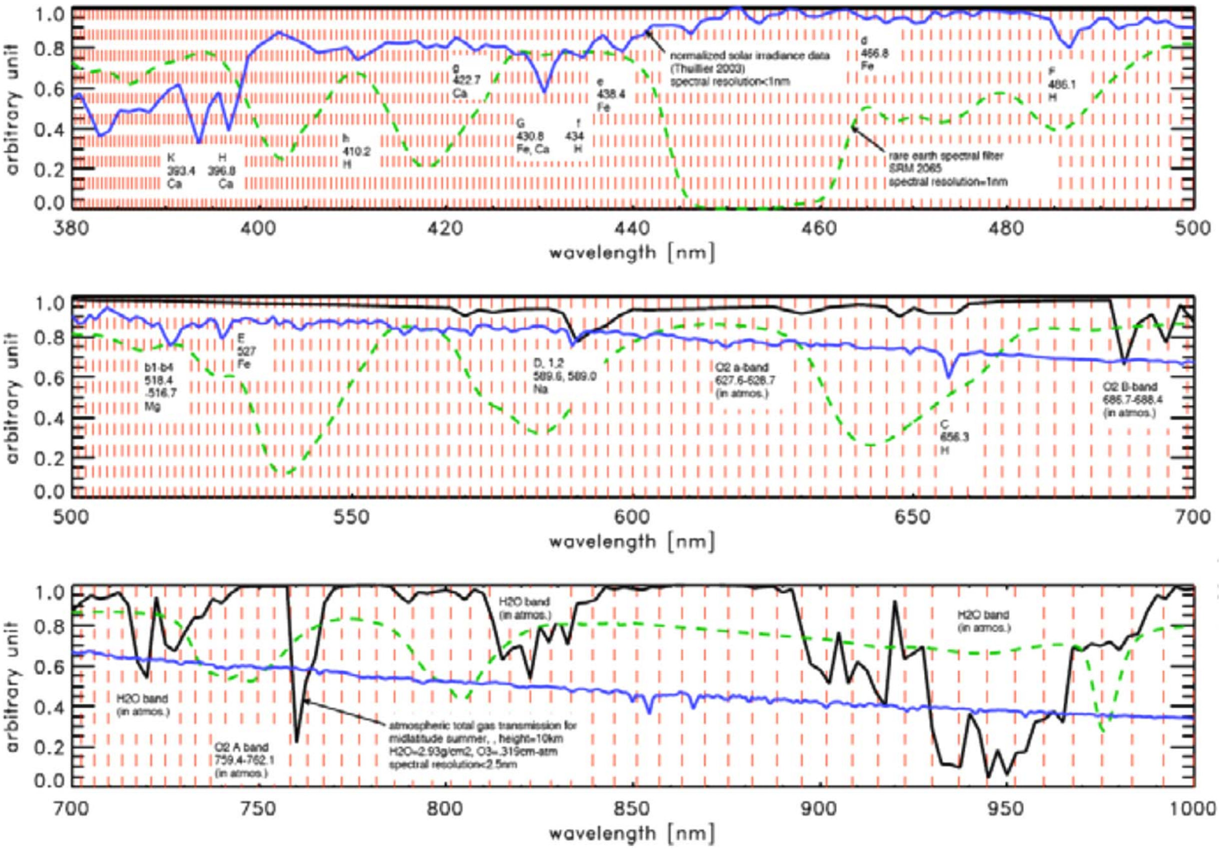

Fig. 3. SRF characterization is integral part of the APEX design using absorption information of the atmosphere (black line), solar light (blue line), and the spectral filters within the IFC. The rare-earth filter is indicated as dashed green line. In the figure, the center wavelength of 312 VNIR spectral bands (before binning) is shown as vertical dashed red lines.

This is particularly true in scenes with characteristics commonly encountered in applications where homogenous areas with high SNR are required, e.g., mining, snow, and agriculture targets.

b) Discernibility of spatial misregistration: Spatial misregistration is an artifact caused either by quadratic optical aberrations and/or misalignments between the components of the scanning system, and it concerns pushbroom spectrometers. Spatial misregistration, if more than 5% of a pixel size, acts in such a way that two spectra, corresponding to two neighboring ground pixels, cannot be distinguished completely.

Recently, a scene-based procedure has been implemented in order to detect spatial misregistration: Edges are first identified on the acquired data, and the variation of their orientation in both wavelength and across-track pixels is then calculated [36].

More in detail, the method recognizes prominent edges within the image and sharpens them in order to increase the contrast. The maxima in the sharpened image are a first good guess on the indication of where the edges can be located. A weighted sum around the maxima, decreasing linearly with the distance from them, is applied in order to achieve subpixel precision. As spatial misregistration depends on the sensed scene, an ideal edge is used as a reference in order to allow correction for such an artifact.

The results demonstrated that spatial misregistration is not constant within the focal plane; it depends quadratically on wavelengths and linearly on across-track positions. This artifact is constant for all the pixels with nadir view (i.e., 0°), and it changes quadratically along the pixels corresponding to other view angles. At a given spectral wavelength, spatial misregistration varies linearly along the pixels corresponding to different view angles. This scene-based procedure has been applied to several hyperspectral sensors, and the analysis (see Table IV) shows that, on average, spatial misregistration is within the requirements for most of the sensors. The table also gives a comparison of keystone in different sensors and the average amount of spatial misregistration in three significant positions along the across-track dimension.

Spatial misregistration as determined by this procedure has also been compared, when possible, with laboratory measurement: Such a comparison gives confidence that this algorithm can be used in a potential correction scheme. Furthermore, the results allow identification of misalignments between the optical components of the sensor.

B. Data Processing

In general, the processing of imaging spectrometers is divided into two basic steps: 1) the retrieval of the calibration and characterization parameters describing the spectral, spatial, and radiometric performance of the instrument; and 2) the processing of calibrated image data products generated by the same instrument using the calibration parameters retrieved during the first step.

TABLE IV
SPATIAL MISREGISTRATION FOR VARIOUS IMAGING SPECTROMETERS, EXPRESSED IN FRACTION OF A PIXEL SIZE AT NADIR AND TWO OFF-NADIR POSITIONS (± FOV/2)

	-FOV/2	NADIR	+ FOV/2
AISA	-0.0343	0.0014	0.0841
AVIRIS VIS	0.0281	0.0112	-0.0184
AVIRIS NIR	0.0188	-0.0099	-0.0054
AVIRIS SWIR1	0.0507	0.0045	-0.0639
AVIRIS SWIR2	0.0452	0.0112	-0.0305
CASI3	0.1004	0.0098	-0.1015
CHRIS	-0.2002	0.0381	0.2569
HYPERION SWIR	0.0511	-0.0028	-0.0232
HYPERION VNIR	0.2261	-0.0046	-0.2296
HYSPEX	0.0629	-0.0025	-0.1039
PHILLS	-0.1405	-0.0029	0.2269

1) Calibration Data Assimilation and Processing: In general, the HSI instrument is calibrated by using different sources such as measurements from the CHB, the IFC, and vicariously retrieved calibration information. For each method, a slightly different set of calibration parameters will be delivered at various times throughout the duration of the mission. For example, the effect of the $R_{\mathrm{AC}}^{\mathrm{PSF}}$ width variation is modeled by convolving the photon flux at detector with a 2-D normalized Gaussian distribution $\sigma_{j,k}$ taking the at-detector coordinates (y_j, z_k) corresponding to continuous pixel indices. Thus, the PSF of the detector pixel (j, k) is calculated as

$$\mathrm{PSF}_{j,k}(y_i, z_k) = \frac{1}{2\pi\sigma_j\sigma_k} \exp\left(-\frac{(y_i - j)^2}{2\sigma_j^2} - \frac{(z_k - k)^2}{2\sigma_k^2}\right). \tag{7}$$

It is characterized by its widths j and k in the two dimensions of the detector. These two parameters are assumed to be constant for columns j, k for the standard forward modeling case.

In addition, the accuracy of the results is not constant, depending on the uncertainties of the measurements. This means that the retrieved calibration parameters must be analyzed in a way to reflect the situation of the HSI instrument at a given time. To find adequate parameters, the time evolution of the parameters from the heterogeneous calibration measurements is retrieved by using a data assimilation technique. This flexible data assimilation algorithm was implemented in the PAF in order to combine the information from all of the heterogeneous calibration measurements, as well as from the system insight. In the data assimilation, a Kalman filter combines the past observations in an optimal way at every instance in time. Under the assumption that the system behaves linearly and that the measurement uncertainty is Gaussian, the Kalman filter performs the conditional probability density propagation as described in [37].

The data assimilation algorithm is pursued during the operational phase of the HSI instrument, monitoring possible upgrades or degradations of the system. The open architecture of the processor allows enhancements to the processor to be done on a regular basis in response to the increasing knowledge of the HSI system's stability and performance.

2) Processing of Image Data: In general, a PAF manages the data from acquisition and calibration to processing and dissemination [28]. The processing chain is based on analyzing in-flight acquired image data, housekeeping information (e.g., navigation data and temperature), and onboard calibration data. Frequent laboratory measurements allow the characterization and calibration of the geometric, radiometric, and spatial sensor parameters. By using the outcome of the sensor calibration, the raw image data are converted to at-sensor radiance, traceable to a certified standard.

By using state-of-the-art technology, a large amount of data (100's of GB) are expected during HSI flight campaigns. Hence, data will undergo an offline chain of data correction and characterization processes based on previously acquired laboratory and in-flight calibration parameters. This processing chain includes conversion of raw data values into SI units, bad pixel replacement, and corrections of smear, straylight, smile, and keystone anomalies. A simplified block diagram of the processing is shown in Fig. 4. The data acquisition process produces the top four components on the left side in the "raw data" column. The lower two components are produced during intermission characterization measurements of the instrument which take place in the laboratory during the flight or vicariously. The analysis of the characterization measurements will result in calibration parameter files consisting of required calibration parameters for L1 processing and quality control. All parameters are accompanied by variances that quantify their uncertainties. In addition, any correlation between the parameters' errors, which may be induced by the instrument characterization procedure, is quantified.

V. SUMMARY AND CONCLUSION

Summarizing the results of the nonuniformity studies from Section III, it is possible to generalize the influences for the HSI assuming the following preconditions: 1) exclusion of worst

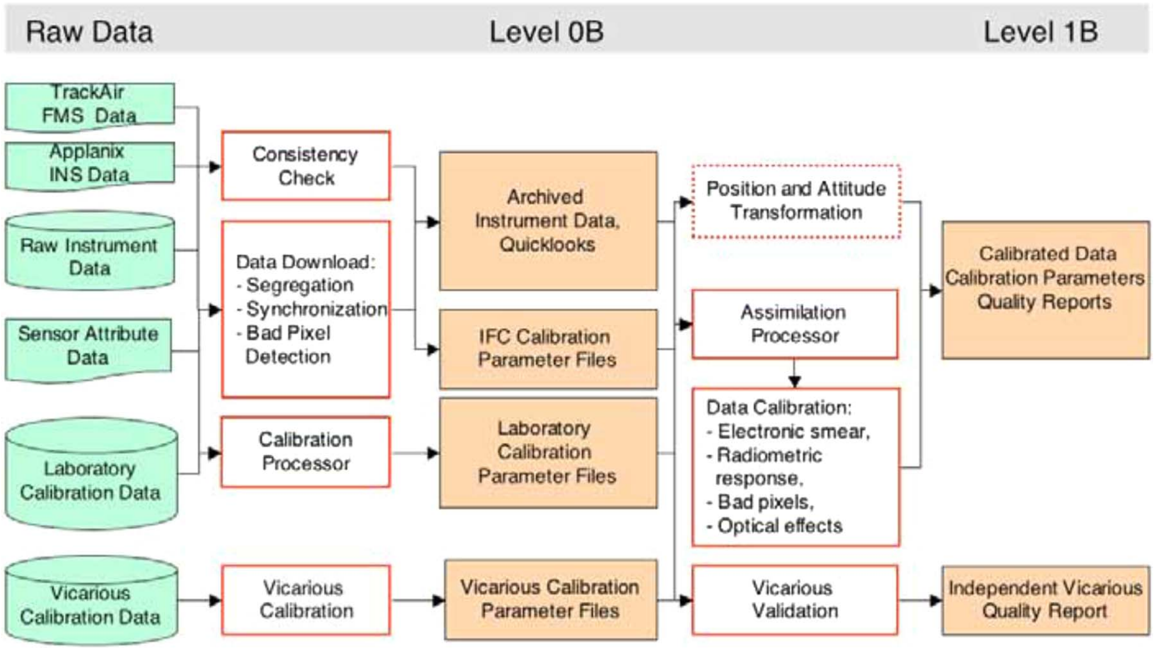

Fig. 4. Generalized processing data flow from raw data until a calibrated at-sensor Level 1B data product.

TABLE V
ESTIMATED AVERAGE IMPACT DUE TO NONUNIFORMITIES IN TERMS OF RMS DEVIATIONS AND ANTICIPATED ERRORS FOR UPCOMING SENSOR GENERATIONS

Defect		Average performance	Average error	Resulting cube error	Anticipated error	Anticipated cube error
Punctual defects				**0.1 %**		**0.1 %**
	punctual	100 bad pixels/frame	5 %		5 %	
	line	1 missing line/frame	5 %		5 %	
Area				**1.4 %**		**0.7 %**
	spatial	0.2 pixel	1 %		0.5 % (0.1 pixel)	0.5 %
	spectral	0.2 pixel	1 %		0.5 % (0.1 pixel)	
Stability		2 % / flight line	2 %	**2 %**	1 %	**1 %**
Degradation		4 % / year	8.9 %	**8.9 %**	2 % (with CHB)	**4.5 %**
Total error (RMS)				**~9.2 %**		**~4.6 %**

case scenarios, such as spectral bands located in absorption band and in the near-UV or far-SWIR; and 2) state-of-the-art correction through raw data preprocessing, such as bad pixel replacement.

Thereafter, it is possible to calculate rms uncertainties for the entire cube (see Table V, column 4), taking the following values for the relevant variables: An HSI provides an imaging cube in the across-track $\times$ spectral $\times$ along-track dimensions with altogether $1000 \times 300 \times 15000 = 4.5$ Gpixels; the lifetime of the sensor should be five years.

As a result, the total rms error of the image cube was calculated reaching the 10% level after five years, even though worst case scenarios were excluded and state-of-the-art correction was applied.

Clearly, uncertainties in the magnitude of 10% for the delivered data are unacceptable, particularly when considering that these calculations are only true for those uncertainties outlined in Section III. Further uncertainties resulting from radiometric (absolute and relative) performance, polarization sensitivities, straylight, and pointing instabilities are not considered in this analysis. Since these errors very much depend on the selected radiance standard and the chosen optical design, these values have not been reflected in the current analysis elaborating the influence of nonuniformities of HSI data products. However, it can be concluded that the magnitude of a resulting absolute-total-cube error could easily approach 15%—also without taking worst case scenarios into account.

In the right part of Table V (column 6), the anticipated image cube error was summarized with the following assumptions:

1) Improvement on the number of bad pixels is detector technology driven and not considered for the improvement of overall data accuracy.
2) Improved optical design will also reduce the spatial and spectral misregistrations to about 0.1 pixel on average, resulting in an improved cube error of 0.7%.
3) The short-term stability of hyperspectral data will be improved by using enhanced monitoring and correction schemes, leading to the 1% limit for a single flight line.
4) Long-term monitoring using further laboratory and scene-based calibration methodologies (as described in Section IV) will allow further reduction to the 2% level per year (or 4.5% over the five-year lifetime).

This table shows an overall error of 4.6% which is mainly driven by the sensor degradation (i.e., the temporal nonuniformity). If the degradation is monitored accurately by calibration means to a level of 2%, the overall error can apparently be reduced to a level below 3%.

In anticipation of the future pushbroom imaging spectrometer missions (e.g., APEX and EnMAP) and its expected applications, this paper has shown the importance of a coordinated method for achieving a maximum of uniformity in data products. This investigation addresses the increasing demand for more reliable data products generated by current and future imaging spectrometer data providers. The data user is able to better understand the impact of a deviation from the perfect data cube, i.e., a nonuniformity of imaging spectrometry data products. This directly leads to the fact that the science community will now be able to quantify the quality of imaging spectrometry data and predict (via error propagation) the uncertainty of their respective higher level processing results and products.

References

[1] J. Nieke and I. Reusen, "A new method to retrieve the data requirements of the remote sensing community—Exemplarily demonstrated for hyperspectral user needs," *Sensors*, vol. 7, pp. 1545–1558, Aug. 2007.

[2] J. Nieke, H. Schwarzer, A. Neumann, and G. Zimmermann, "Imaging spaceborne and airborne sensor systems in the beginning of the next century," *Proc. SPIE*, vol. 3221, pp. 581–592, Dec. 1997.

[3] M. A. Folkman, J. Pearlman, B. L. Liao, and P. J. Jarecke, "EO-1/Hyperion hyperspectral imager design, development, characterization, and calibration," *Proc. SPIE*, vol. 4151, pp. 40–51, Feb. 2001.

[4] M. A. Cutter, "A small satellite hyperspectral mission," in *Proc. 4S Symp. Small Satell., Syst. Services*, La Rochelle, France, Sep. 20–24, 2004. SP571.

[5] S. K. Babey and C. D. Anger, "Compact airborne spectrographic imager (CASI): A progress review," *Proc. SPIE*, vol. 1937, pp. 152–163, Sep. 1993.

[6] T. G. Chrien, R. O. Green, and M. L. Eastwood, "Accuracy of the spectral and radiometric laboratory calibration of the Airborne Visible/Infrared Imaging Spectrometer (AVIRIS)," in *Proc. SPIE—Imaging Spectroscopy of the Terrestrial Environment*, 1990, vol. 1298, pp. 37–49.

[7] R. Bärs, L. Watson, and O. Weatherbee, "AISA as a tool for timely commercial remote sensing," in *Proc. 4th Int. Airborne Remote Sens. Conf. Exhib., Ottawa, ON, Canada*. Ann Arbor, MI: ERIM, 1999, vol. I, pp. 239–246.

[8] T. Cocks, R. Jenssen, A. Stewart, I. Wilson, and T. Shields, "The Hymap airborne hyperspectral sensor: The system, calibration and performance," in *Proc. 1st EARSeL Workshop Imaging Spectrosc.*, Zurich, Switzerland, 1998, pp. 37–42.

[9] J. Nieke, K. I. Itten, and W. Debruyn, "The airborne imaging spectrometer APEX: From concept to realization," in *Proc. 4th EARSeL Workshop Imaging Spectrosc.*, Warsaw, Poland, 2005.

[10] A. Müller, R. Richter, M. Habermeyer, H. Mehl, S. Dech, H. J. Kaufmann, K. Segl, P. Strobl, P. Haschberger, and R. Bamler, "ARES: A new reflective/emissive imaging spectrometer for terrestrial applications," *Proc. SPIE*, vol. 5574, pp. 120–127, Oct. 2004.

[11] H. Kaufmann, K. Segl, S. Chabrillat, S. Hofer, T. Stuffler, A. Mueller, R. Richter, G. Schreier, R. Haydn, and H. Bach, "EnMAP a hyperspectral sensor for environmental mapping and analysis," in *Proc. IGARSS*, 2006, pp. 1617–1619.

[12] I. E. Abdou and N. J. Dusaussoy, "Survey of image quality measurements," in *Proc. Fall Joint Comput. Conf.*, Dallas, TX, Nov. 2–6, 1986, pp. 71–78.

[13] D. Kavaldjiev and Z. Ninkov, "Influence of nonuniform charge-coupled device pixel response on aperture photometry," *Opt. Eng.*, vol. 40, no. 2, pp. 162–169, Feb. 2001.

[14] D. Schläpfer, J. Nieke, and K. I. Itten, "Spatial PSF non-uniformity effects in airborne pushbroom imaging spectrometry data," *IEEE Trans. Geosci. Remote Sens.*, vol. 45, no. 2, pp. 458–468, Feb. 2007.

[15] J. Nieke, M. Solbrig, and N. Neumann, "Noise contributions for imaging spectrometers," *Appl. Opt.*, vol. 38, no. 24, pp. 5191–5194, Aug. 1999.

[16] P. Mouroulis, R. O. Green, and T. G. Chrien, "Design of pushbroom imaging spectrometers for optimum recovery of spectroscopic and spatial information," *Appl. Opt.*, vol. 39, no. 13, pp. 2210–2220, May 2000.

[17] S. Bojinski, M. Schaepman, D. Schläpfer, and K. Itten, "SPECCHIO: A spectrum database for remote sensing applications," *Comput. Geosci.*, vol. 29, no. 1, pp. 27–38, Feb. 2003.

[18] A. Hüni, J. Nieke, J. Schopfer, M. Kneubühler, and K. I. Itten, "The spectral database SPECCHIO for improved long term usability and data sharing," *Comput. Geosci.*, 2007. to be published.

[19] A. Berk, L. Berstein, G. Anderson, P. Acharya, D. Robertson, J. Chetwynd, and S. Adler-Golden, "MODTRAN cloud and multiple scattering upgrades with applications to AVIRIS," *Remote Sens. Environ.*, vol. 65, no. 3, pp. 367–375, 1998.

[20] D. Schläpfer, M. Schaepman, and P. Strobl, "Impact of spatial resampling methods on the radiometric accuracy of airborne imaging spectrometer data," in *Proc. 5th Int. Airborne Remote Sens. Conf. Exhib.*, San Francisco, CA, 2001, p. 8. CD-ROM.

[21] D. Schläpfer, J. Nieke, and K. I. Itten, *APEX Performance Assessment*, p. 52, 2006. Internal ESA Report APEX_RSL_CON05.

[22] J. Nieke, J. Kaiser, D. Schläpfer, J. Brazile, K. Itten, P. Strobl, M. Schaepman, and G. Ulbrich, "Calibration methodology for the airborne dispersive pushbroom imaging spectrometer (APEX)," *Proc. SPIE*, vol. 5570, pp. 445–452, 2004.

[23] H. Kaufmann, S. Chabrillat, S. Mannheim, N. Richter, K. Segl, M. Dees, R. Haydn, M. Lautner, A. Müller, R. Richter, S. Hofer, I. Chorus, P. Hostert, F. Jung-Rothenhäusler, F. Kühn, and M. Sommer, *EnMAP, Environmental Mapping and Analysis Program—User Requirements Document*, 2005. Third Issue (21.06.2005) by GeoForschungsZentrum Potsdam (GFZ), Gesellschaft für Angewandte Fernerkundung AG (GAF), Deutsches Zentrum für Luft- und Raumfahrt (DLR).

[24] G. Ulbrich, *APEX SoW for Phase C/D*, Apr. 5, 2002. ESA document, EOP-FI/2002-04-631/GU/gu.

[25] B.-C. Gao, K. B. Heidebrecht, and A. F. H. Goetz, "Derivation of scaled surface reflectances from AVIRIS data," *Remote Sens. Environ.*, vol. 44, no. 2/3, pp. 165–178, Jun. 1993.

[26] K. Staenz, J. Secker, B.-C. Gao, C. Davis, and C. Nadeau, "Radiative transfer codes applied to hyperspectral data for the retrieval of surface reflectance," *ISPRS J. Photogramm. Remote Sens.*, vol. 57, no. 3, pp. 194–203, Dec. 2002.

[27] D. Schläpfer, M. Schaepman, S. Bojinski, and A. Börner, "Calibration and validation concept for the airborne prism experiment (APEX)," *Can. J. Remote Sens.*, vol. 26, no. 5, pp. 455–465, 2000.

[28] A. Hueni, J. Biesemans, K. Meuleman, F. Dell'Endice, D. Odermatt, D. Schlaepfer, M. Kneubuehler, S. Adriaensen, S. Kempenaers, J. Nieke, and K. Itten, "Structure, components and interfaces of the Airborne Prism Experiment (APEX) processing and archiving facility," *IEEE Trans. Geosci. Remote Sens.*, 2008. to be published.

[29] P. Gege, J. Fries, P. Haschberger, P. Schötz, H. Schwarzer, P. Strobl, B. Suhr, G. Ulbrich, and W. J. Vreeling, "Calibration facility for airborne imaging spectrometers," *ISPRS J. Photogramm. Remote Sens.*, 2007. to be published.

[30] B.-C. Gao, M. J. Montes, and C. O. Davis, "Refinement of wavelength calibrations of hyperspectral imaging data using a spectrum-matching technique," *Remote Sens. Environ.*, vol. 90, no. 4, pp. 424–433, Apr. 2004.

[31] R. A. Neville, L. Sun, and K. Staenz, "Detection of spectral line curvature in imaging spectrometer data," *Proc. SPIE*, vol. 5093, pp. 144–154, Sep. 2003.

[32] D. Ramon, R. P. Santer, and P. Dubuisson, "MERIS in-flight spectral calibration in O_2 absorption using surface pressure retrieval," *Proc. SPIE*, vol. 4891, pp. 505–514, Apr. 2003.

[33] D. G. Goodenough, A. Dyk, O. Niemann, J. S. Pearlman, H. Chen, T. Han, M. Murdoch, and C. West, "Processing Hyperion and ALI for forest classification," *IEEE Trans. Geosci. Remote Sens.*, vol. 41, no. 6, pp. 1321–1331, Jun. 2003.

[34] J. Brazile, R. A. Neville, K. Staenz, D. Schläpfer, L. Sun, and K. I. Itten, "Scene-based spectral response function shape discernibility for the APEX imaging spectrometer," *IEEE Geosci. Remote Sens. Lett.*, vol. 3, no. 3, pp. 414–418, Jul. 2006.

[35] J. Brazile, R. A. Neville, K. Staenz, D. Schläpfer, L. Sun, and K. I. Itten, "Toward scene-based retrieval of spectral response for hyperspectral imagers using Fraunhofer features," *Can. J. Remote Sens.*, 2007. to be published.

[36] F. Dell'Endice, J. Nieke, D. Schläpfer, and K. I. Itten, "Scene-based method for spatial misregistration detection in hyperspectral imagery," *Appl. Opt.*, vol. 46, no. 15, pp. 2803–2816, May 2007.

[37] J. W. Kaiser, D. Schläpfer, J. Brazile, P. Strobl, and M. E. Schaepman, "Assimilation of heterogeneous calibration measurements for the APEX spectrometer," *Proc. SPIE*, vol. 5234, pp. 211–220, Feb. 2003.

Jens Nieke received the M.Eng. degree in aeroc and astronautical engineering from the Technical University of Berlin, Berlin, Germany, and National Institute of Applied Sciences (INSA), Lyon, France, and the Ph.D. degree on an advanced satellite mission study for regional coastal zone monitoring from the Technical University of Berlin in 2001.

In 1995, he joined the MOS-IRS Team, German Aerospace Center, Berlin, which launched a spaceborne imaging spectrometer in 1997. From 2000 to 2003, he was a Visiting Scientist with the Earth Observation Research Center, Japan Aerospace Exploration Agency, Tokyo, Japan, involved in the calibration and validation of the ADEOS-II GLI mission. From 2004 to 2007, he was with the Remote Sensing Laboratories, University of Zurich, Zurich, Switzerland, as a Senior Scientist, Lecturer, and Project Manager of the Airborne Prism EXperiment (APEX) project of the European Space Agency (ESA). Since 2007, he has been with the ESA at the European Space Research and Technology Centre, Noordwijk, Netherlands, where he is member of the Sentinel-3 team.

Daniel Schläpfer received the M.Sc. degree in geography, the Ph.D. (Dr.sc.nat.) degree, and the teaching degree in physics and geography from the University of Zurich, Zurich, Switzerland, in 1994, 1998, and 1999, respectively.

He is currently a Research Associate with the Remote Sensing Laboratories, University of Zurich, and a Consultant to and a Processing Scientist with the European Space Agency's Airborne Prism EXperiment. In addition, he is a Professor of physics with Kantonsschule Wil, Wil, Switzerland. His current scientific work focuses on the implementation of sophisticated tools for the processing and validation of imaging spectrometry data. He owns and runs the company ReSe Applications Schläpfer, Wil, which is a company focused on the development and distribution of the imaging spectroscopy software packages PARGE, MODO, and ATCOR. His major fields of research are atmospheric and geometric preprocessing of hyperspectral data.

Francesco Dell'Endice received the master's degree in aerospace engineering from the Politecnico di Milano, Milano, Italy, the Dipl.Ing. degree in spacecraft and vehicles from the Ecole Superieure de l'Aeronatique et de l'Espace (SUPAERO), Toulouse, France, and a graduate certificate in applied science (space studies) from the International Space University (Strasbourg, France)–University of South Australia (Adelaide, Australia). He is currently working toward the Ph.D. degree in remote sensing at the Remote Sensing Laboratories, University of Zurich, Zurich, Switzerland, with a special interest in the calibration of hyperspectral imaging spectrometers.

He is a member of the Airborne Prism EXperiment (APEX) Team, responsible for the calibration concept.

Jason Brazile received the B.A. degree in computer science from the University of North Texas, Denton, in 1991, the M.S. degree in computer science from the University of Texas, Austin, in 1994, and the Ph.D. degree in natural sciences from the University of Zurich, Zurich, Switzerland, in 2008.

He joined the Airborne Prism EXperiment (APEX) Team, Remote Sensing Laboratories, University of Zurich, in 2002, where he worked on the parallel and distributed implementation of calibration and preprocessing algorithms in support to the production of APEX imaging spectrometer data products.

Klaus I. Itten (M'82–SM'97) received the M.Sc. and Ph.D. degrees in geography from the University of Zurich, Zurich, Switzerland, in 1969 and 1973, respectively.

Since 1982, he has been a Professor in geography and remote sensing with the University of Zurich. As the Head of the Remote Sensing Laboratories, his research and teaching interests are remote sensing and image processing for natural resources inventorying and monitoring. In particular, the application of optical remote sensing and high-spatial- and high-spectral-resolution image data and analysis are the focus of his research. As the Principal Investigator for the APEX project, imaging spectroscopy and spectroradiometry have become important parts of his endeavors.

Uniformity of Imaging Spectrometry Data Products

Jens Nieke, Daniel Schläpfer, Francesco Dell'Endice, Jason Brazile, and Klaus I. Itten, *Senior Member, IEEE*

***Abstract*—The increasing quantity and sophistication of imaging spectroscopy applications have led to a higher demand on the quality of Earth observation data products. In particular, it is desired that data products be as consistent as possible (i.e., ideally uniform) in both spectral and spatial dimensions. Yet, data acquired from real (e.g., pushbroom) imaging spectrometers are adversely affected by various categories of artifacts and aberrations including as follows: singular and linear (e.g., bad pixels and missing lines), area (e.g., optical aberrations), and stability and degradation defects. Typically, the consumer of such data products is not aware of the magnitude of such inherent data uncertainties even as more uncertainty is introduced during higher level processing for any particular application. In this paper, it is shown that the impact of imaging spectrometry data product imperfections in currently available data products has an inherent uncertainty of 10%, even though worst case scenarios were excluded, state-of-the-art corrections were applied, and radiometric calibration uncertainties were excluded. Thereafter, it is demonstrated how this error can be reduced ($< 5\%$) with appropriate available technology (onboard, scene, and laboratory calibration) and assimilation procedures during the preprocessing of the data. As a result, more accurate, i.e., uniform, imaging spectrometry data can be delivered to the user community. Hence, the term uniformity of imaging spectrometry data products is defined for enabling the quantitative means to assess the quality of imaging spectrometry data. It is argued that such rigor is necessary for calculating the error propagation of respective higher level processing results and products.**

***Index Terms*—Calibration, data processing, imaging, spectroscopy.**

I. Introduction

Since the first airborne hyperspectral imagers (HSIs) were developed in the 1980s, significant effort has been devoted to increase the quality of the resulting hyperspectral data cube. Today, it can be stated that the use of hyperspectral data found its way from prototyping to commercial applications resulting in an increasing demand on highly accurate measurements to satisfy the needs of hyperspectral data user community [1]. In general, a hyperspectral data cube is typically generated by a pushbroom- or whiskbroom-type imaging spectrometer in order to enable the registration in the three dimensions of the cube, i.e., spectral, first spatial (across-track), and second spatial time (along-track) domains [2]. Examples for selected currently operational [3]–[8] and soon-to-be-available HSI [9]–[11] are given in the Table I.

Even though HSI instrument development and its data application have long history, error estimations for the entire data cube were not established so far—mainly due to the lack of detailed performance specifications on the manufacturer side and the nescience of the consequence of relaxed (or nonexisting) requirements on the user side.

In order to better understand the quality of the HSI data products, a thorough understanding of nonuniformities of the data and their corresponding correction schemes needs to be elaborated.

This is why this paper specifically performs the following:

1) addresses the HSI instrument model, which was developed at Remote Sensing Laboratories (RSL) in order to account for the error contributions of data nonuniformities appropriately;
2) describes the source and impact of uniformities artifacts on the HSI data products quality;
3) outlines possible characterization, calibration, and correction schemes;
4) summarizes the overall impact on the HSI product and gives estimates on anticipated errors.

II. Instrument Model

An appropriate HSI instrument model F is introduced for serving as a forward model in order to solve the inverse problem of data processing as well as that of instrument calibration.

The instrument model must reproduce the instrument's behavior accurately. This is why, first, the common equation of signal transformations is provided. The transformation converts the digital numbers C inside the instrument to the radiance field L_s

$$C = F * L_s \tag{1}$$

where the symbol $*$ represents the convolution operator.

Due to the higher transformation complexity of a pushbroom-like HSI, only this kind of instrument is addressed in this paper. In an HSI optical system, the photons of the radiance at sensor L_s are distributed among the pixels of the detector in both the spectral and the across-track directions. The forward movement of the instrument over the scene and the detector's integration time—together with high frequency read-out—allows generation of a hyperspectral data cube.

The instrument model consists of the system's pixel response function $R_{\mathrm{sys}}^{\mathrm{PRF}}$ and various other calibration and characterization parameters (such as polarization sensitivity, ghost and

Manuscript received June 4, 2007; revised September 29, 2007. First published Month 00, 0000; last published Month 00, 0000 (projected).

J. Nieke is with the European Space Agency (ESA), European Space Research and Technology Centre, 2200 Noordwijk, Netherlands.

D. Schläpfer is with the Remote Sensing Laboratories (RSL), University of Zurich, 8057 Zurich, Switzerland, and also with Kantonsschule Wil, 9501 Wil, Switzerland.

F. Dell'Endice, J. Brazile, and K. I. Itten are with the Remote Sensing Laboratories (RSL), University of Zurich, 8057 Zurich, Switzerland.

Color versions of one or more of the figures in this paper are available online at http://ieeexplore.ieee.org.

Digital Object Identifier 10.1109/TGRS.2008.918764

TABLE I
SPECIFICATIONS AND DESIGN PARAMETERS FOR CURRENT AND FUTURE HYPERSPECTRAL IMAGERS

HSI [manufacturer, country/agency]	Year of 1st operations	No. of Spectr. Bands	Spectr. Range (µm)	Spectr. Resolution (λ/Δλ)	FOV [deg] IFOV [mrad]	Imaging Technique
Airborne IS						
AVIRIS [JPL, US]	1987	224	0.4 - 2.5	40-200	30° 1 mrad	1D whisk., grating
CASI [ITRES, CA]	1990	288	0.4 - 1.0	200	40° 1.5 mrad	2D push., grating
HYMAP [Intergrated Spectronics, AU]	1994	128	0.4 - 2.5	30-125	65° 2 mrad	1D whisk., grating
AISA Eagle [SPECIM, FI]	2005	244	0.4 - 0.97	200-300	39.7° 1 mrad	2D push., prism
ARES [Intergrated Spectronics, AU/DLR]	from 2007	128 (VIS-SWIR); 30 (TIR)	0.4-2.5 8-12	30-125 64-100	65° 2 mrad	1D whisk., grating
APEX [RUAG, ESA/CH/BE]	from 2008	313-500	0.38 - 2.5	1000-277	28° 0.5 mrad	2D push., prism
Spaceborne IS						
HYPERION [Northrop Grumman, NASA]	2000	200	0.4 - 2.5	40-250	7.5 km, 30 m	2D push., grating
CHRIS [SSTL, ESA]	2001	18-62	0.4 - 1.0	300-90	13km, 17-34 m	2D push., prism
EnMAP [Keyser Threde, GFZ, DLR]	from 2012	220	0.43 - 2.5	43-250	30km, 30m	2D push., prism

straylight effects, and the absolute radiometric accuracy) combined in the variable K_{sys}

$$F = R_{\mathrm{sys}}^{\mathrm{PRF}} * K_{\mathrm{sys}}. \tag{2}$$

Assuming a linear system, the $R_{\mathrm{sys}}^{\mathrm{PRF}}$ can be expressed as a multiple convolution of point spread functions (PSFs), each associated with one of the system components (e.g., the optics, detectors, and signal and data processing).

In the case of a pushbroom imaging spectrometer, the image of one line is redistributed at the detector level in the spectral (λ) and first spatial (θ) domains. Together with the along-track movement (given by the time t) of the sensor (second spatial domain), we define two spatial PSFs ($R_{\mathrm{AC}}^{\mathrm{PSF}}$ and $R_{\mathrm{AL}}^{\mathrm{PSF}}$) and the spectrometer-inherent spectral response function (SRF) $(R_{\lambda}^{\mathrm{SRF}})$. The convolution of the normalized PSFs (in a way that the 2-D integral over the two-orthogonal distance variables is equal to one) and the $R_{\lambda}^{\mathrm{SRF}}$ results in the pixel response function $(R_{\mathrm{IS}}^{\mathrm{PRF}})$

$$R_{\mathrm{IS}}^{\mathrm{PRF}} = R_{\mathrm{AC}}^{\mathrm{PRF}} * R_{\mathrm{AL}}^{\mathrm{PRF}} * R_{\lambda}^{\mathrm{SRF}} \tag{3}$$

where $R_{\mathrm{AC}}^{\mathrm{PSF}}$ and $R_{\mathrm{AL}}^{\mathrm{PSF}}$ correspond to the across-track (indices AC) and along-track (indices AL) PSFs.

Hence, $R_{\mathrm{IS}}^{\mathrm{PRF}}$ is the spatial map of sensitivity across a pixel as well as the information about the crosstalk between neighboring pixels over the entire detector at a certain wavelength λ.

Now, the relation for the HSI needs to be expressed mathematically. In contrast to classical camera design models [12], [13], an HSI model must also account for the spectral domain, resulting in an incident image intensity distribution represented by $f(x, y, z)$, with the pixel response function $r(x, y, z)$ and the signal $s(t, \lambda, \Theta)$ being detected by the pixel (i, j, k) and given as

$$s(i,j,k) = \iiint_{-\infty}^{+\infty} L_s(t,\lambda,\theta) F_{i,j,k}(t,\lambda,\theta)\, dt\, d\lambda\, d\theta \tag{4}$$

on the level of the detector.

The data are already influenced by the optics, and therefore, the different equation based on the image density function $f(x, y, z)$ applies

$$s(i,j,k) = \iiint_{-\infty}^{+\infty} R_{\mathrm{sys}}^{\mathrm{PRF}}(x,y,z) f(x,y,z)\, dx\, dy\, dz \tag{5}$$

where the coordinate system is defined with reference to the detector.

The R^{PRF} resulting from the convolutions in the two spatial and the spectral domains is a good basis to assess the quality of HSI data. Here, the shape, the size, and the diameter of the central lobe are not only related to the spectral and spatial resolutions but also to the sharpness in 3-D of the image cube produced. An ideal R^{PRF} would have a constant value within the boundaries of a pixel (i.e., uniform pixel sensitivity) and

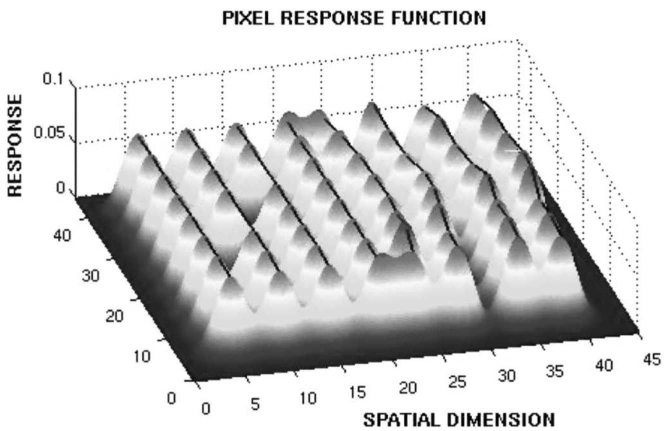

(a)

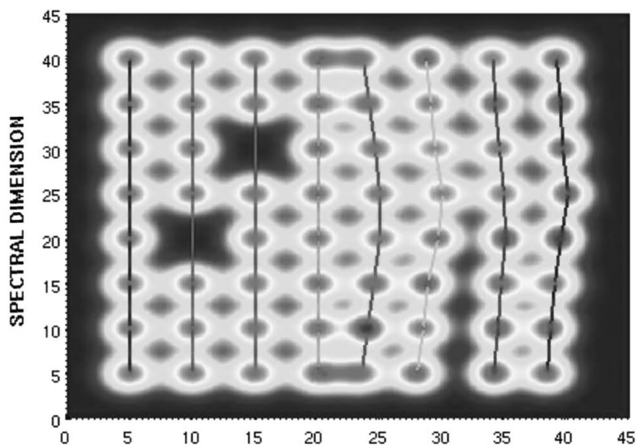

(b)

Fig. 1. 3-D view (a) and top view (b) of PRF for eight across-track pixels and eight spectral bands before the 2-D detector array. On the left side, 4 × 8 PRFs are uniform except of two bad pixels. In contrast, keystone (or spatial misregistration) as nonuniformity is affecting the image quality of 4 × 8 PRFs on the right side.

zero outside (i.e., no crosstalk or oversampling). However, in practice, instrument data show intrapixel sensitivity variations and nonuniformities in the detector domains (see Figs. 1 and 2). This is why real sensors' PRFs are, in general, simplified as Gaussian functions and not as boxcar functions—the Gaussian distribution more closely matches the description of real sensors. However, we have to keep in mind that the Gaussian PSF is still a simplification. The differences to a real PSF can be estimated comparing the function shapes in Fig. 1 for Gaussian and Fig. 2 for real system distributions.

For the components of R^{PRF} to be measured, various techniques can be applied. Whereas monochromators, tunable lasers, echelons, or absorption filters can be used for R^{SRF} determination, the characterizations of $R_{\mathrm{AC}}^{\mathrm{PSF}}$ and $R_{\mathrm{AL}}^{\mathrm{PSF}}$ are more complex. A favorable way is to characterize the PSF via a line spread function (LSF) (R^{LSF}) or an edge spread function (R^{ESF}). In contrast to the PSF, which can be regarded as a two-dim response to an input point source, the one-dim LSF is determined by a line that is infinitely long and narrow. However, either an R^{LSF} or R^{ESF} exists for each line or edge orientation. Assuming that $R_{\mathrm{AC}}^{\mathrm{PSF}}(y,z)$ represents the response at a point of the spatial coordinate (y,z) and that $R_{\mathrm{AC}}^{\mathrm{LSF}}(y')$

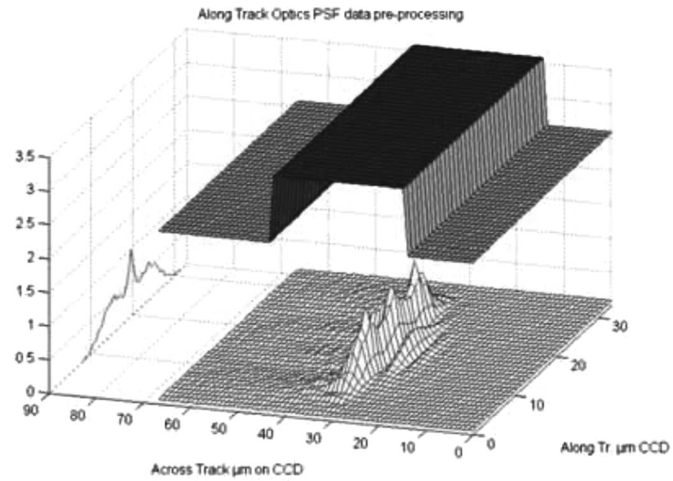

Fig. 2. Typical PSFs as an $R_{\mathrm{AC}}^{\mathrm{PSF}} * R_{\mathrm{AL}}^{\mathrm{PSF}}$ convolution for an imaging spectrometer at $\mathrm{FOV} = 14^\circ$ and $\lambda = 400$ nm.

represents the LSF for a line of orientation z', where y' is orthogonal to z', then the LSF is the integral of the $R_{\mathrm{AL}}^{\mathrm{PSF}}$ in the z'-direction

$$R^{\mathrm{LSF}}(y') = \int_{-\infty}^{+\infty} R_{\mathrm{AC}}^{\mathrm{PSF}}(y,z)\,dz'. \tag{6}$$

The straightforward consequence of (1)–(6) is that $R_{\mathrm{IS}}^{\mathrm{PRF}}$ should be exactly known in order to decompose the measured data C into a sum of point sources with known spatial and spectral profiles, i.e., the quantitative assessment of the quality of HSI data.

To better understand the influence of possible imperfections of a homogenous or uniform distribution of equal $R_{\mathrm{IS}}^{\mathrm{PRF}}$, it is important to define the artifacts and aberrations in HSI data and their consequences more precisely.

III. Impact of Uniformity Defects on Imaging Spectrometry Data Products

A. *Uniformity Definition*

Two uniformity terms are commonly used for the description of artifacts in electronic imaging, i.e., spatial uniformity and temporal uniformity.

1) Spatial uniformity: For spatial uniformity, the radiometric response is defined as equality within a (spatial) frame detector. This term primarily stems from frame imaging, e.g., in digital photography. It includes effects such as striping or spectrally variable radiometric response related to varying quantum efficiency within a detector array.
2) Temporal uniformity: The temporal uniformity describes the temporal radiometric response stability of a detector element. This term is common in video analysis and is used synonymously with "radiometric stability" in imaging spectroscopy.

In contrast to those definitions, pushbroom imaging spectrometry consists of one image frame registering the spectral and the spatial dimension simultaneously. Any nonuniformity in the system PSF (i.e., the PSF nonuniformity) leads therefore to nonuniformities of the data products in both the spectral and spatial dimensions [14]. Such nonuniformities are commonly termed smile and keystone, respectively. This is why the term uniformity of imaging spectrometry data products must be introduced.

B. *Uniformity of Imaging Spectrometry Data Products*

In order to reduce the $R_{\mathrm{IS}}^{\mathrm{PRF}}$ nonuniformity of HSI data, major efforts on data preprocessing and analysis have to be taken into account. The following types of imperfections are defined as nonuniformities, assuming the pixel as a point.

1) Singular defects, where the $R_{\mathrm{IS}}^{\mathrm{PRF}}$ of a single pixel is significantly lower (e.g., 50%) than the mean response of the surrounding detector pixels (e.g., "bad pixels"). Also, all intrapixel nonuniformities are singular defects that are not to be neglected for HSI data preprocessing.
2) Linear defects, where the response of an entire line is affected (e.g., "striping," missing lines) or smear [15].
3) Area defects, where the entire frame has imperfections, which are mainly formed by optical aberrations and sampling inconsistencies in the spectral and the first spatial domain. The result is a PSF nonuniformity through spectral and spatial misregistrations which correspond to smile and keystone within one detector array [16].
4) Stability defects, where the entire image cube (including the temporal dimension) is affected by, e.g., nonstability of an instrument. These defects typically result in deviations in the second spatial (along-track) domain during the flight.
5) Discontinuity defects are caused through the degradation of the HSI through stepwise deteriorations in the optics and/or electronics of the instrument. This defect may cause misinterpretations of temporal effects and time series.

C. *Impact of Nonuniformity*

After defining the nonuniformity of imaging spectrometry data, it is important to quantify the impact of the PSF nonuniformity on data processing. The most prominent effects have been analyzed recently, i.e., $R_{\mathrm{AC}}^{\mathrm{PSF}}$ variation, coregistration, and spectral stability, using test data, which were systematically convolved to standard $R_{\mathrm{AC}}^{\mathrm{PSF}}$ values. The root mean square (rms) of the radiance difference between deviating PSFs and an ideal PSF was derived from such simulated data, which resulted in relative error percentages. As test data, various spectral data cubes were used, such as artificial data cubes derived from the SPECCHIO spectral database [17], [18], where a wide range of more than 4000 natural and simulated surface reflectance spectra had been modeled to at-sensor radiance data using the MODTRAN radiative transfer code [19], or a number of real imaging spectrometry (e.g., from AVIRIS) test data sets. The results from the different analyses [14], [20] are summarized in the following.

1) Singular and Linear Defects: The correction of singular pixel defects was tested by linear interpolation of missing pixels from neighboring pixels. The average error of the bilinear interpolation method to the original pixel value was between 11% and 19% for the replacement of individual pixels, dependent on the wavelength and the interpolation method. If the interpolation was done in the spectral domain, this error was reduced below 5% for spectrally highly resolved instruments. The deviations with nearest neighbor processing were stable at about 17.5%. Bilinear interpolation performed better than nearest neighbor replacement techniques by a factor of up to two if only individual pixels have to be replaced. Singular defects could not be corrected by interpolation beyond a distance of two to three pixels for high-resolution imagery [20].

2) Area PSF Defects: For HSI, the spatial PSF width is ideally 1.0 and, typically, is slightly blurred to higher values assuming a contiguous sampling. A variation of the PSF width of 1–1.6 pixels in the across-track direction and 1.2–1.6 pixels in the along-track dimension across the full spectral range was investigated. The influence on the data is in the range of 1%–4% [14]. The results for PSF variations showed that higher resolution of low altitude imagery increases the errors significantly—this indicates that the highest resolution imagery will be even more critical.

Spatial coregistration between the two detectors (e.g., for a visible and infrared channel) can be defective due to pressure- or temperature-dependent misregistrations. In fact, this is a special case of area defects and may be treated by similar procedures. The misregistration effect is quantified as the standard deviation of the difference between resampled imagery using ideal and distorted sensor models. Relative differences of at-sensor radiance reaching 10% were observed between the two sensor models for an arbitrary collection of spectra. To improve the situation, across-track linear interpolation was applied to distorted data (at the same spatial resolution) in order to recover the original image positions. The linear interpolation reduced the error to a level of 2% [20].

3) Stability Defects: The stability of HSI is mainly driven by pressure/temperature dependencies resulting from flight level variations from airborne systems and solar heat forcing on the sensor during a single orbit for spaceborne systems. Deviations from uniformity may be observed in the data up to a corresponding estimated level of 10% (compare Table V). The quantification of this defect is technically feasible using an onboard characterization means and the HSI instrument model. A relative accuracy (i.e., stability) level of 2% is achievable by onboard characterization and subsequent data calibration—in case these instabilities are actually encountered [21], [22].

4) Discontinuity Defects: Discontinuities of system performance are by nature unforeseeable (e.g., degradation of optical performances) in their impact on system performance. It is assumed that laboratory or in-flight performance monitoring will allow tracing the system performance after a discontinuity has been encountered, e.g., after an unexpected shift of the system parameters. Except for a short transition phase, laboratory or in-flight calibration will allow a complete update of the system characterization. Depending on the performance of in-flight monitoring, a 2% error level can be reached, at the latest after a new laboratory characterization [20].

TABLE II
ESTIMATED IMPACT IN TERMS OF RMS DEVIATIONS DUE TO NONUNIFORMITIES FOR THE APEX INSTRUMENT

Non-Uniformity	Maximum Error	Corrected Error
Point / Line	16%	5%
Area: spatial PSF	4%	1%
Area: spectral PSF	5%	1%
Shortterm Stability	10%	2%
Longterm Discont.	50%	2%
Total RMS	**52.90%**	**6.3%**

TABLE III
TYPICAL TECHNICAL REQUIREMENTS FOR STATE-OF-THE-ART HSI [23], [24].

Dimension	Technical Requirement	EnMAP	APEX
Spectral	Spectral Misregistration	< 0.2 pixels	< 0.2 pixels
	Spectral Stability	< 0.5 nm	< 0.1 nm
Spatial	Spatial Misregistration	< 0.2 pixels	< 0.16 pixels
	Coregistration error (VNIR-SWIR)		< 0.16 pixels
General	Relative radiometric stability		< 2%

5) Error Budget: Such derived relative errors due to the different nonuniformity effects can be scaled to the actual performance of a specific HSI using a linear relationship between nonuniformity value and expected error. Given the expected radiometric performance of current systems (e.g., those mentioned in Table I), a residual inaccuracy in the range of 2% [21] is achievable for short-term stability only and remains a challenging goal for operational long-term use of the instrument.

In Table II, the impact of nonuniformities is summarized for the most prominent effects in terms of relative data errors as worst case maximum error and corrected error estimates. The residual error is large even after corrections are applied. It only falls below 4% if bad pixels are not part of the error budget or if considerably improved correction schemes are developed for all kinds of nonuniformities.

D. Typical Uniformity Requirements for HSI Data Products

The state of the art of technical requirements for PSF-related issues for HSI is quite difficult to determine since these values were not discussed in detail within the HSI user community so far. This is why just some state-of-the-art requirements can be summarized resulting from two exemplary sensors (Table III). Those values combined with the values retrieved from existing instruments using scene-based characterization methods (Section IV) will be used in Section V as average performance values.

IV. INSTRUMENT AND DATA CALIBRATION

Since the early steps of HSI calibration, important steps in the quantification of HSI nonuniformities have been performed [25], [26]. In order to deliver high-quality data products, it is necessary to quantify the defect and, thereafter, calibrate the flight data appropriately. These steps are called instrument calibration and data calibration. The realization is carried out during various calibration cycles and a processing of the flight data using the retrieved calibration parameters. In the following, an exemplary approach is described on how HSI instrument and data calibration is performed [22], [27] and the subsequent processing [28] is provided. This approach has been tested with various HSI data sets; it is also generic, i.e., can be used for different HSI sensors.

A. Calibration Measurements

First, the HSI instrument model F and the related parameters have to be described appropriately. Therefore, it is necessary to perform a large variety of calibration and characterization measurements applying different methods, e.g., onboard characterization, frequent laboratory characterization, and vicarious calibration. The retrieved parameters allow data calibration in a processing and archiving facility (PAF). The data calibration includes the calculation of the required time-dependent calibration coefficients from the calibration parameters and, subsequently, the radiometric, spectral, and geometric calibrations of the raw data. Because of the heterogeneity of the characterization measurements, the optimal calibration for each data set is achieved by using a special assimilation algorithm. In order to demonstrate state-of-the-art calibration technology, the characteristics of the recently developed calibration facilities are summarized in the following sections. Serving as examples are the APEX in-flight characterization (IFC) [22], [29] and the APEX calibration home base (CHB) facilities, which were recently developed and allow accurate PRF characterization measurements for providing input for the subsequent processing and assimilation scheme.

1) Onboard Performance Monitoring: As an integral part of an HSI, an onboard performance monitor can be used to perform characterization measurements using a filter wheel consisting of various filters, which permits spectral and radiometric characterization. The spectral filters are a rare-earth filter and three bandpass filters at 694, 1000, and 2218 nm. IFC design and performance were described recently [22], and it was shown that the IFC is capable of characterizing the spectral band center with an accuracy of < 1 nm together with a radiometric stability of $< 0.5\%$ as relative error. IFC measurements are performed before and after each run (flight line with continuous uninterrupted data acquisition) and during the CHB calibration measurements.

2) CHB: The CHB with dedicated spectral, radiometric, and geometric calibration facilities allows full laboratory characterization and calibration of HSI. The CHB is located at DLR in Oberpfaffenhofen near Munich (Germany).

The CHB consists of a large integrating sphere (1.6-m diameter) to enable radiometric calibration and an optical bench for the spatial and spectral calibrations of APEX. The entire setup makes use of a highly stable design mechanism, such as a rigid granite optical bench, a perfectly isolated foundation (seismic block), and special air bearings. This is why high positioning accuracy in the range of micrometers and arc seconds can be guaranteed. Details on the special design realized for the calibration bench, the integrating sphere, and the interfaces, as well as the large variety of possible spectral, geometric, radiometric, polarimetric, and straylight-related characterization measurements, are given in [29]. For the determination of APEX's PRF, the following measurements are performed: SRF and across/along-track LSF characterization.

For the SRF, a two-step procedure is applied. In the first step, the stimulus from a monochromatic source is geometrically centered on a detector column by equalizing the signal from neighboring elements. In the second step, the SRFs of the elements in this column are scanned by the stepwise increase or decrease of the wavelength of the stimulus. For each element, the integration time should be individually optimized by APEX to suppress noise and achieve best possible results.

Spatially, the characterization will be performed in along- and across-track directions by measuring the R^{LSF} simultaneously using the panchromatic beam of the collimator. For the characterization of the entire matrix detector, the measurements have to be performed for different angular positions across the swath.

For the along-track $R^{\mathrm{LSF}}_{\mathrm{AL}}$, the measurement will be accomplished by shifting a vertical slit (perpendicular to the one used for the across-track $R^{\mathrm{LSF}}_{\mathrm{AC}}$) in the focal plane of the collimator slightly left and right, i.e., in along-track direction. This movement will be realized by a rotating slit wheel, as the rotational component of such a small shift is negligible. The LSF for the across-track characterization is measured in steps of 1°, i.e., performing 29 steps from -14° to $+14^\circ$.

It has been recently shown [29] that the resulting accuracies of R^{LSF} and R^{SRF} characterizations are in the range of < 0.1 pixels leading to very small uncertainties with regard to spectral (± 0.1 nm) and geometric (± 0.007 mrad) calibrations.

3) Vicarious or Scene-Based Calibration: In-orbit vicarious or scene-based calibration is an important tool for monitoring an instrument's performance throughout the mission's duration. Along with the measurement of radiometric features, spectral R^{SRF} and spatial PSF characterizations and/or refinement can be performed as well. In support of the aforementioned uniformity goals, the latter two (R^{SRF} and R^{PSF}) are more critical and, therefore, led to a more detailed investigation. Based on proofs of concept, it has been shown that both R^{SRF} (i.e., band center, bandwidth, and R^{SRF} shape) and spatial misregistration (i.e., keystone) characterizations are possible in most cases. This is of special interest for addressing HSI nonuniformity issues, particularly for those instruments where characterization is only performed once throughout the entire mission duration, i.e., during the prelaunch calibration activities.

a) Spectral misregistration: While the scene-based retrieval of band center and bandwidth is well described in literature [30]–[34], recently, the discernibility of per-band SRF parameters has been explored using imaging spectrometry data [34]. It was demonstrated that various instrument R^{SRF} shapes could be discerned from a scene by measuring the difference between HSI data and various theoretical R^{SRF} (Gaussian, Bartlett, cosine, Welch, and box).

In particular, to establish discernibility, feature windows for comparison of 75 MODTRAN-4 cases (five target reflectances $\times$ three visibilities $\times$ five R^{SRF}) were selected from among candidate Fraunhofer lines determined to have prominent features: K (Ca), H (Ca), G (Fe), C (H), B (O_2), and A (O_2) (see Fig. 3). For each candidate feature, all window sizes ranging from two to five bands on each side of the feature were iteratively evaluated to choose the "best" window. The window size was then fixed for that particular feature, and an iterative window selection procedure allowed tuning the selection of features that are most suitable for a particular instrument.

In this investigation, it was shown that the Bartlett R^{SRF} is generally the least discernible from the Gaussian R^{SRF}; the A (O_2) and B (O_2) features seem to have the lowest signal-to-noise (SNR) requirements for discernment; the seemingly very similar cosine and Welch R^{SRF} appear to be easily discernible when compared against the Gaussian; and finally, differing visibility and target reflectance values have mostly minor influences on discernibility.

Based on the establishment of discernibility under these conditions, a method for direct R^{SRF} retrieval was then developed assuming less theoretical R^{SRF} shapes and tested over a wider variety of instrument performance characteristics [35]. Promising results were seen under simulation conditions, allowing variation of parameters over hundreds of permutations based on models of three currently available imaging spectrometers.

Promising results were seen under simulation conditions, allowing variation of parameters over hundreds of permutations based on models of the CHRIS, Hymap, and Hyperion imaging spectrometers, even though their realization of the feature window sizes and locations relative to the actual feature centers varied greatly. Many features proved usable with SNR performance as low as $5000:1$, which is easily achievable by averaging samples of topologically invariable homogeneous targets, since SNR is improved by the square root of the number of samples taken. Even in its currently primitive form, the described method could be used to obtain SRF estimates better than the typically used Gaussian for the not-uncommon case in which bands are created by summing up to tens of subchannels.

In summary, an instrument's R^{SRF} shape can now be added along with the already established bandwidth and band center in the list of spectral characteristics that can be retrieved or at least refined from the spectrometry data.

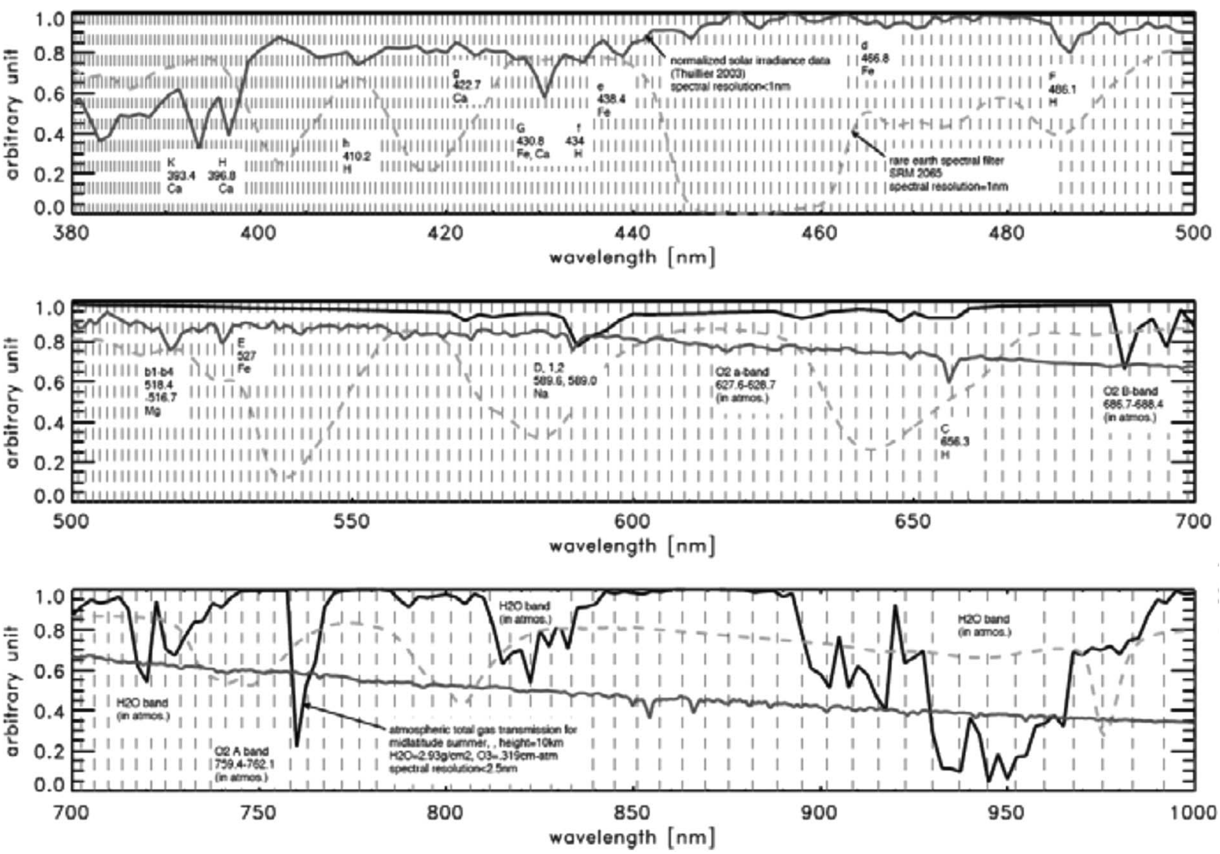

Fig. 3. SRF characterization is integral part of the APEX design using absorption information of the atmosphere (black line), solar light (blue line), and the spectral filters within the IFC. The rare-earth filter is indicated as dashed green line. In the figure, the center wavelength of 312 VNIR spectral bands (before binning) is shown as vertical dashed red lines.

This is particularly true in scenes with characteristics commonly encountered in applications where homogenous areas with high SNR are required, e.g., mining, snow, and agriculture targets.

b) Discernibility of spatial misregistration: Spatial misregistration is an artifact caused either by quadratic optical aberrations and/or misalignments between the components of the scanning system, and it concerns pushbroom spectrometers. Spatial misregistration, if more than 5% of a pixel size, acts in such a way that two spectra, corresponding to two neighboring ground pixels, cannot be distinguished completely.

Recently, a scene-based procedure has been implemented in order to detect spatial misregistration: Edges are first identified on the acquired data, and the variation of their orientation in both wavelength and across-track pixels is then calculated [36]. More in detail, the method recognizes prominent edges within the image and sharpens them in order to increase the contrast. The maxima in the sharpened image are a first good guess on the indication of where the edges can be located. A weighted sum around the maxima, decreasing linearly with the distance from them, is applied in order to achieve subpixel precision. As spatial misregistration depends on the sensed scene, an ideal edge is used as a reference in order to allow correction for such an artifact.

The results demonstrated that spatial misregistration is not constant within the focal plane; it depends quadratically on wavelengths and linearly on across-track positions. This artifact is constant for all the pixels with nadir view (i.e., 0°), and it changes quadratically along the pixels corresponding to other view angles. At a given spectral wavelength, spatial misregistration varies linearly along the pixels corresponding to different view angles. This scene-based procedure has been applied to several hyperspectral sensors, and the analysis (see Table IV) shows that, on average, spatial misregistration is within the requirements for most of the sensors. The table also gives a comparison of keystone in different sensors and the average amount of spatial misregistration in three significant positions along the across-track dimension.

Spatial misregistration as determined by this procedure has also been compared, when possible, with laboratory measurement: Such a comparison gives confidence that this algorithm can be used in a potential correction scheme. Furthermore, the results allow identification of misalignments between the optical components of the sensor.

B. Data Processing

In general, the processing of imaging spectrometers is divided into two basic steps: 1) the retrieval of the calibration and characterization parameters describing the spectral, spatial, and radiometric performance of the instrument; and 2) the processing of calibrated image data products generated by the same instrument using the calibration parameters retrieved during the first step.

TABLE IV
SPATIAL MISREGISTRATION FOR VARIOUS IMAGING SPECTROMETERS, EXPRESSED IN FRACTION OF A PIXEL SIZE AT NADIR AND TWO OFF-NADIR POSITIONS (± FOV/2)

	-FOV/2	NADIR	+ FOV/2
AISA	-0.0343	0.0014	0.0841
AVIRIS VIS	0.0281	0.0112	-0.0184
AVIRIS NIR	0.0188	-0.0099	-0.0054
AVIRIS SWIR1	0.0507	0.0045	-0.0639
AVIRIS SWIR2	0.0452	0.0112	-0.0305
CASI3	0.1004	0.0098	-0.1015
CHRIS	-0.2002	0.0381	0.2569
HYPERION SWIR	0.0511	-0.0028	-0.0232
HYPERION VNIR	0.2261	-0.0046	-0.2296
HYSPEX	0.0629	-0.0025	-0.1039
PHILLS	-0.1405	-0.0029	0.2269

1) Calibration Data Assimilation and Processing: In general, the HSI instrument is calibrated by using different sources such as measurements from the CHB, the IFC, and vicariously retrieved calibration information. For each method, a slightly different set of calibration parameters will be delivered at various times throughout the duration of the mission. For example, the effect of the $R_{\mathrm{AC}}^{\mathrm{PSF}}$ width variation is modeled by convolving the photon flux at detector with a 2-D normalized Gaussian distribution $\sigma_{j,k}$ taking the at-detector coordinates (y_j, z_k) corresponding to continuous pixel indices. Thus, the PSF of the detector pixel (j, k) is calculated as

$$\mathrm{PSF}_{j,k}(y_i, z_k) = \frac{1}{2\pi\sigma_j\sigma_k} \exp\left(-\frac{(y_i - j)^2}{2\sigma_j^2} - \frac{(z_k - k)^2}{2\sigma_k^2}\right). \tag{7}$$

It is characterized by its widths j and k in the two dimensions of the detector. These two parameters are assumed to be constant for columns j, k for the standard forward modeling case.

In addition, the accuracy of the results is not constant, depending on the uncertainties of the measurements. This means that the retrieved calibration parameters must be analyzed in a way to reflect the situation of the HSI instrument at a given time. To find adequate parameters, the time evolution of the parameters from the heterogeneous calibration measurements is retrieved by using a data assimilation technique. This flexible data assimilation algorithm was implemented in the PAF in order to combine the information from all of the heterogeneous calibration measurements, as well as from the system insight. In the data assimilation, a Kalman filter combines the past observations in an optimal way at every instance in time. Under the assumption that the system behaves linearly and that the measurement uncertainty is Gaussian, the Kalman filter performs the conditional probability density propagation as described in [37].

The data assimilation algorithm is pursued during the operational phase of the HSI instrument, monitoring possible upgrades or degradations of the system. The open architecture of the processor allows enhancements to the processor to be done on a regular basis in response to the increasing knowledge of the HSI system's stability and performance.

2) Processing of Image Data: In general, a PAF manages the data from acquisition and calibration to processing and dissemination [28]. The processing chain is based on analyzing in-flight acquired image data, housekeeping information (e.g., navigation data and temperature), and onboard calibration data. Frequent laboratory measurements allow the characterization and calibration of the geometric, radiometric, and spatial sensor parameters. By using the outcome of the sensor calibration, the raw image data are converted to at-sensor radiance, traceable to a certified standard.

By using state-of-the-art technology, a large amount of data (100's of GB) are expected during HSI flight campaigns. Hence, data will undergo an offline chain of data correction and characterization processes based on previously acquired laboratory and in-flight calibration parameters. This processing chain includes conversion of raw data values into SI units, bad pixel replacement, and corrections of smear, straylight, smile, and keystone anomalies. A simplified block diagram of the processing is shown in Fig. 4. The data acquisition process produces the top four components on the left side in the "raw data" column. The lower two components are produced during intermission characterization measurements of the instrument which take place in the laboratory during the flight or vicariously. The analysis of the characterization measurements will result in calibration parameter files consisting of required calibration parameters for L1 processing and quality control. All parameters are accompanied by variances that quantify their uncertainties. In addition, any correlation between the parameters' errors, which may be induced by the instrument characterization procedure, is quantified.

V. SUMMARY AND CONCLUSION

Summarizing the results of the nonuniformity studies from Section III, it is possible to generalize the influences for the HSI assuming the following preconditions: 1) exclusion of worst

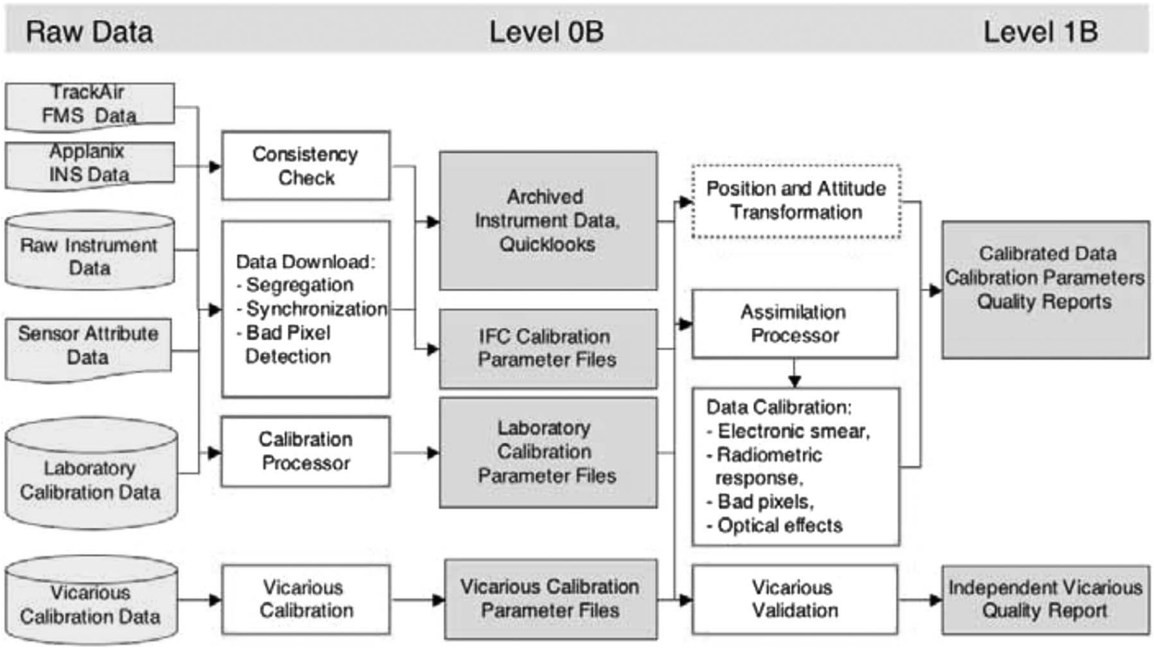

Fig. 4. Generalized processing data flow from raw data until a calibrated at-sensor Level 1B data product.

TABLE V
ESTIMATED AVERAGE IMPACT DUE TO NONUNIFORMITIES IN TERMS OF RMS DEVIATIONS AND ANTICIPATED ERRORS FOR UPCOMING SENSOR GENERATIONS

Defect		Average performance	Average error	Resulting cube error	Anticipated error	Anticipated cube error
Punctual defects				**0.1 %**		**0.1 %**
	punctual	100 bad pixels/frame	5 %		5 %	
	line	1 missing line/frame	5 %		5 %	
Area				**1.4 %**		**0.7 %**
	spatial	0.2 pixel	1 %		0.5 % (0.1 pixel)	0.5 %
	spectral	0.2 pixel	1 %		0.5 % (0.1 pixel)	
Stability		2 % / flight line	2 %	**2 %**	1 %	**1 %**
Degradation		4 % / year	8.9 %	**8.9 %**	2 % (with CHB)	**4.5 %**
Total error (RMS)				**~9.2 %**		**~4.6 %**

case scenarios, such as spectral bands located in absorption band and in the near-UV or far-SWIR; and 2) state-of-the-art correction through raw data preprocessing, such as bad pixel replacement.

Thereafter, it is possible to calculate rms uncertainties for the entire cube (see Table V, column 4), taking the following values for the relevant variables: An HSI provides an imaging cube in the across-track $\times$ spectral $\times$ along-track dimensions with altogether $1000 \times 300 \times 15000 = 4.5$ Gpixels; the lifetime of the sensor should be five years.

As a result, the total rms error of the image cube was calculated reaching the 10% level after five years, even though worst case scenarios were excluded and state-of-the-art correction was applied.

Clearly, uncertainties in the magnitude of 10% for the delivered data are unacceptable, particularly when considering that these calculations are only true for those uncertainties outlined in Section III. Further uncertainties resulting from radiometric (absolute and relative) performance, polarization sensitivities, straylight, and pointing instabilities are not considered in this analysis. Since these errors very much depend on the selected radiance standard and the chosen optical design, these values have not been reflected in the current analysis elaborating the influence of nonuniformities of HSI data products. However, it can be concluded that the magnitude of a resulting absolute-total-cube error could easily approach 15%—also without taking worst case scenarios into account.

In the right part of Table V (column 6), the anticipated image cube error was summarized with the following assumptions:

1) Improvement on the number of bad pixels is detector technology driven and not considered for the improvement of overall data accuracy.
2) Improved optical design will also reduce the spatial and spectral misregistrations to about 0.1 pixel on average, resulting in an improved cube error of 0.7%.
3) The short-term stability of hyperspectral data will be improved by using enhanced monitoring and correction schemes, leading to the 1% limit for a single flight line.
4) Long-term monitoring using further laboratory and scene-based calibration methodologies (as described in Section IV) will allow further reduction to the 2% level per year (or 4.5% over the five-year lifetime).

This table shows an overall error of 4.6% which is mainly driven by the sensor degradation (i.e., the temporal nonuniformity). If the degradation is monitored accurately by calibration means to a level of 2%, the overall error can apparently be reduced to a level below 3%.

In anticipation of the future pushbroom imaging spectrometer missions (e.g., APEX and EnMAP) and its expected applications, this paper has shown the importance of a coordinated method for achieving a maximum of uniformity in data products. This investigation addresses the increasing demand for more reliable data products generated by current and future imaging spectrometer data providers. The data user is able to better understand the impact of a deviation from the perfect data cube, i.e., a nonuniformity of imaging spectrometry data products. This directly leads to the fact that the science community will now be able to quantify the quality of imaging spectrometry data and predict (via error propagation) the uncertainty of their respective higher level processing results and products.

References

[1] J. Nieke and I. Reusen, "A new method to retrieve the data requirements of the remote sensing community—Exemplarily demonstrated for hyperspectral user needs," *Sensors*, vol. 7, pp. 1545–1558, Aug. 2007.

[2] J. Nieke, H. Schwarzer, A. Neumann, and G. Zimmermann, "Imaging spaceborne and airborne sensor systems in the beginning of the next century," *Proc. SPIE*, vol. 3221, pp. 581–592, Dec. 1997.

[3] M. A. Folkman, J. Pearlman, B. L. Liao, and P. J. Jarecke, "EO-1/Hyperion hyperspectral imager design, development, characterization, and calibration," *Proc. SPIE*, vol. 4151, pp. 40–51, Feb. 2001.

[4] M. A. Cutter, "A small satellite hyperspectral mission," in *Proc. 4S Symp. Small Satell., Syst. Services*, La Rochelle, France, Sep. 20–24, 2004. SP571.

[5] S. K. Babey and C. D. Anger, "Compact airborne spectrographic imager (CASI): A progress review," *Proc. SPIE*, vol. 1937, pp. 152–163, Sep. 1993.

[6] T. G. Chrien, R. O. Green, and M. L. Eastwood, "Accuracy of the spectral and radiometric laboratory calibration of the Airborne Visible/Infrared Imaging Spectrometer (AVIRIS)," in *Proc. SPIE—Imaging Spectroscopy of the Terrestrial Environment*, 1990, vol. 1298, pp. 37–49.

[7] R. Bärs, L. Watson, and O. Weatherbee, "AISA as a tool for timely commercial remote sensing," in *Proc. 4th Int. Airborne Remote Sens. Conf. Exhib., Ottawa, ON, Canada*. Ann Arbor, MI: ERIM, 1999, vol. I, pp. 239–246.

[8] T. Cocks, R. Jenssen, A. Stewart, I. Wilson, and T. Shields, "The Hymap airborne hyperspectral sensor: The system, calibration and performance," in *Proc. 1st EARSeL Workshop Imaging Spectrosc.*, Zurich, Switzerland, 1998, pp. 37–42.

[9] J. Nieke, K. I. Itten, and W. Debruyn, "The airborne imaging spectrometer APEX: From concept to realization," in *Proc. 4th EARSeL Workshop Imaging Spectrosc.*, Warsaw, Poland, 2005.

[10] A. Müller, R. Richter, M. Habermeyer, H. Mehl, S. Dech, H. J. Kaufmann, K. Segl, P. Strobl, P. Haschberger, and R. Bamler, "ARES: A new reflective/emissive imaging spectrometer for terrestrial applications," *Proc. SPIE*, vol. 5574, pp. 120–127, Oct. 2004.

[11] H. Kaufmann, K. Segl, S. Chabrillat, S. Hofer, T. Stuffler, A. Mueller, R. Richter, G. Schreier, R. Haydn, and H. Bach, "EnMAP a hyperspectral sensor for environmental mapping and analysis," in *Proc. IGARSS*, 2006, pp. 1617–1619.

[12] I. E. Abdou and N. J. Dusaussoy, "Survey of image quality measurements," in *Proc. Fall Joint Comput. Conf.*, Dallas, TX, Nov. 2–6, 1986, pp. 71–78.

[13] D. Kavaldjiev and Z. Ninkov, "Influence of nonuniform charge-coupled device pixel response on aperture photometry," *Opt. Eng.*, vol. 40, no. 2, pp. 162–169, Feb. 2001.

[14] D. Schläpfer, J. Nieke, and K. I. Itten, "Spatial PSF non-uniformity effects in airborne pushbroom imaging spectrometry data," *IEEE Trans. Geosci. Remote Sens.*, vol. 45, no. 2, pp. 458–468, Feb. 2007.

[15] J. Nieke, M. Solbrig, and N. Neumann, "Noise contributions for imaging spectrometers," *Appl. Opt.*, vol. 38, no. 24, pp. 5191–5194, Aug. 1999.

[16] P. Mouroulis, R. O. Green, and T. G. Chrien, "Design of pushbroom imaging spectrometers for optimum recovery of spectroscopic and spatial information," *Appl. Opt.*, vol. 39, no. 13, pp. 2210–2220, May 2000.

[17] S. Bojinski, M. Schaepman, D. Schläpfer, and K. Itten, "SPECCHIO: A spectrum database for remote sensing applications," *Comput. Geosci.*, vol. 29, no. 1, pp. 27–38, Feb. 2003.

[18] A. Hüni, J. Nieke, J. Schopfer, M. Kneubühler, and K. I. Itten, "The spectral database SPECCHIO for improved long term usability and data sharing," *Comput. Geosci.*, 2007. to be published.

[19] A. Berk, L. Berstein, G. Anderson, P. Acharya, D. Robertson, J. Chetwynd, and S. Adler-Golden, "MODTRAN cloud and multiple scattering upgrades with applications to AVIRIS," *Remote Sens. Environ.*, vol. 65, no. 3, pp. 367–375, 1998.

[20] D. Schläpfer, M. Schaepman, and P. Strobl, "Impact of spatial resampling methods on the radiometric accuracy of airborne imaging spectrometer data," in *Proc. 5th Int. Airborne Remote Sens. Conf. Exhib.*, San Francisco, CA, 2001, p. 8. CD-ROM.

[21] D. Schläpfer, J. Nieke, and K. I. Itten, *APEX Performance Assessment*, p. 52, 2006. Internal ESA Report APEX_RSL_CON05.

[22] J. Nieke, J. Kaiser, D. Schläpfer, J. Brazile, K. Itten, P. Strobl, M. Schaepman, and G. Ulbrich, "Calibration methodology for the airborne dispersive pushbroom imaging spectrometer (APEX)," *Proc. SPIE*, vol. 5570, pp. 445–452, 2004.

[23] H. Kaufmann, S. Chabrillat, S. Mannheim, N. Richter, K. Segl, M. Dees, R. Haydn, M. Lautner, A. Müller, R. Richter, S. Hofer, I. Chorus, P. Hostert, F. Jung-Rothenhäusler, F. Kühn, and M. Sommer, *EnMAP, Environmental Mapping and Analysis Program—User Requirements Document*, 2005. Third Issue (21.06.2005) by GeoForschungsZentrum Potsdam (GFZ), Gesellschaft für Angewandte Fernerkundung AG (GAF), Deutsches Zentrum für Luft- und Raumfahrt (DLR).

[24] G. Ulbrich, *APEX SoW for Phase C/D*, Apr. 5, 2002. ESA document, EOP-FI/2002-04-631/GU/gu.

[25] B.-C. Gao, K. B. Heidebrecht, and A. F. H. Goetz, "Derivation of scaled surface reflectances from AVIRIS data," *Remote Sens. Environ.*, vol. 44, no. 2/3, pp. 165–178, Jun. 1993.

[26] K. Staenz, J. Secker, B.-C. Gao, C. Davis, and C. Nadeau, "Radiative transfer codes applied to hyperspectral data for the retrieval of surface reflectance," *ISPRS J. Photogramm. Remote Sens.*, vol. 57, no. 3, pp. 194–203, Dec. 2002.

[27] D. Schläpfer, M. Schaepman, S. Bojinski, and A. Börner, “Calibration and validation concept for the airborne prism experiment (APEX),” *Can. J. Remote Sens.*, vol. 26, no. 5, pp. 455–465, 2000.

[28] A. Hueni, J. Biesemans, K. Meuleman, F. Dell’Endice, D. Odermatt, D. Schlaepfer, M. Kneubuehler, S. Adriaensen, S. Kempenaers, J. Nieke, and K. Itten, “Structure, components and interfaces of the Airborne Prism Experiment (APEX) processing and archiving facility,” *IEEE Trans. Geosci. Remote Sens.*, 2008. to be published.

[29] P. Gege, J. Fries, P. Haschberger, P. Schötz, H. Schwarzer, P. Strobl, B. Suhr, G. Ulbrich, and W. J. Vreeling, “Calibration facility for airborne imaging spectrometers,” *ISPRS J. Photogramm. Remote Sens.*, 2007. to be published.

[30] B.-C. Gao, M. J. Montes, and C. O. Davis, “Refinement of wavelength calibrations of hyperspectral imaging data using a spectrum-matching technique,” *Remote Sens. Environ.*, vol. 90, no. 4, pp. 424–433, Apr. 2004.

[31] R. A. Neville, L. Sun, and K. Staenz, “Detection of spectral line curvature in imaging spectrometer data,” *Proc. SPIE*, vol. 5093, pp. 144–154, Sep. 2003.

[32] D. Ramon, R. P. Santer, and P. Dubuisson, “MERIS in-flight spectral calibration in O_2 absorption using surface pressure retrieval,” *Proc. SPIE*, vol. 4891, pp. 505–514, Apr. 2003.

[33] D. G. Goodenough, A. Dyk, O. Niemann, J. S. Pearlman, H. Chen, T. Han, M. Murdoch, and C. West, “Processing Hyperion and ALI for forest classification,” *IEEE Trans. Geosci. Remote Sens.*, vol. 41, no. 6, pp. 1321–1331, Jun. 2003.

[34] J. Brazile, R. A. Neville, K. Staenz, D. Schläpfer, L. Sun, and K. I. Itten, “Scene-based spectral response function shape discernibility for the APEX imaging spectrometer,” *IEEE Geosci. Remote Sens. Lett.*, vol. 3, no. 3, pp. 414–418, Jul. 2006.

[35] J. Brazile, R. A. Neville, K. Staenz, D. Schläpfer, L. Sun, and K. I. Itten, “Toward scene-based retrieval of spectral response for hyperspectral imagers using Fraunhofer features,” *Can. J. Remote Sens.*, 2007. to be published.

[36] F. Dell’Endice, J. Nieke, D. Schläpfer, and K. I. Itten, “Scene-based method for spatial misregistration detection in hyperspectral imagery,” *Appl. Opt.*, vol. 46, no. 15, pp. 2803–2816, May 2007.

[37] J. W. Kaiser, D. Schläpfer, J. Brazile, P. Strobl, and M. E. Schaepman, “Assimilation of heterogeneous calibration measurements for the APEX spectrometer,” *Proc. SPIE*, vol. 5234, pp. 211–220, Feb. 2003.

Jens Nieke received the M.Eng. degree in aeroc and astronautical engineering from the Technical University of Berlin, Berlin, Germany, and National Institute of Applied Sciences (INSA), Lyon, France, and the Ph.D. degree on an advanced satellite mission study for regional coastal zone monitoring from the Technical University of Berlin in 2001.

In 1995, he joined the MOS-IRS Team, German Aerospace Center, Berlin, which launched a spaceborne imaging spectrometer in 1997. From 2000 to 2003, he was a Visiting Scientist with the Earth Observation Research Center, Japan Aerospace Exploration Agency, Tokyo, Japan, involved in the calibration and validation of the ADEOS-II GLI mission. From 2004 to 2007, he was with the Remote Sensing Laboratories, University of Zurich, Zurich, Switzerland, as a Senior Scientist, Lecturer, and Project Manager of the Airborne Prism EXperiment (APEX) project of the European Space Agency (ESA). Since 2007, he has been with the ESA at the European Space Research and Technology Centre, Noordwijk, Netherlands, where he is member of the Sentinel-3 team.

Daniel Schläpfer received the M.Sc. degree in geography, the Ph.D. (Dr.sc.nat.) degree, and the teaching degree in physics and geography from the University of Zurich, Zurich, Switzerland, in 1994, 1998, and 1999, respectively.

He is currently a Research Associate with the Remote Sensing Laboratories, University of Zurich, and a Consultant to and a Processing Scientist with the European Space Agency’s Airborne Prism EXperiment. In addition, he is a Professor of physics with Kantonsschule Wil, Wil, Switzerland. His current scientific work focuses on the implementation of sophisticated tools for the processing and validation of imaging spectrometry data. He owns and runs the company ReSe Applications Schläpfer, Wil, which is a company focused on the development and distribution of the imaging spectroscopy software packages PARGE, MODO, and ATCOR. His major fields of research are atmospheric and geometric preprocessing of hyperspectral data.

Francesco Dell’Endice received the master’s degree in aerospace engineering from the Politecnico di Milano, Milano, Italy, the Dipl.Ing. degree in spacecraft and vehicles from the Ecole Superieure de l’Aeronatique et de l’Espace (SUPAERO), Toulouse, France, and a graduate certificate in applied science (space studies) from the International Space University (Strasbourg, France)–University of South Australia (Adelaide, Australia). He is currently working toward the Ph.D. degree in remote sensing at the Remote Sensing Laboratories, University of Zurich, Zurich, Switzerland, with a special interest in the calibration of hyperspectral imaging spectrometers.

He is a member of the Airborne Prism EXperiment (APEX) Team, responsible for the calibration concept.

Jason Brazile received the B.A. degree in computer science from the University of North Texas, Denton, in 1991, the M.S. degree in computer science from the University of Texas, Austin, in 1994, and the Ph.D. degree in natural sciences from the University of Zurich, Zurich, Switzerland, in 2008.

He joined the Airborne Prism EXperiment (APEX) Team, Remote Sensing Laboratories, University of Zurich, in 2002, where he worked on the parallel and distributed implementation of calibration and preprocessing algorithms in support to the production of APEX imaging spectrometer data products.

Klaus I. Itten (M’82–SM’97) received the M.Sc. and Ph.D. degrees in geography from the University of Zurich, Zurich, Switzerland, in 1969 and 1973, respectively.

Since 1982, he has been a Professor in geography and remote sensing with the University of Zurich. As the Head of the Remote Sensing Laboratories, his research and teaching interests are remote sensing and image processing for natural resources inventorying and monitoring. In particular, the application of optical remote sensing and high-spatial- and high-spectral-resolution image data and analysis are the focus of his research. As the Principal Investigator for the APEX project, imaging spectroscopy and spectroradiometry have become important parts of his endeavors.